

TRASE: Tracking-free 4D Segmentation and Editing

Yun-Jin Li^{*1}

Mariia Gladkova^{*1,2†}

Yan Xia^{1,2}

Daniel Cremers^{1,2}

¹ TU Munich ² Munich Center for Machine Learning

{yunjin.li, mariia.gladkova, yan.xia, cremers}@tum.de

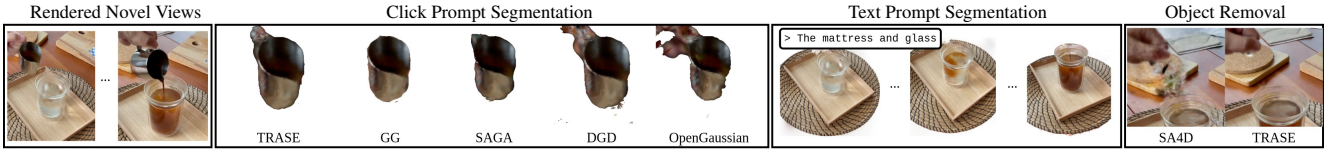


Figure 1. We propose TRASE, a novel tracking-free 4D segmentation approach. TRASE achieves superior object segmentation from click prompts and further supports interactive editing tasks such as object removal and text-prompt-based segmentation.

Abstract

Understanding dynamic 3D scenes is crucial for extended reality (XR) and autonomous driving. Incorporating semantic information into 3D reconstruction enables holistic scene representations, unlocking immersive and interactive applications. To this end, we introduce TRASE, a novel tracking-free 4D segmentation method for dynamic scene understanding. TRASE learns a 4D segmentation feature field in a weakly-supervised manner, leveraging a soft-mined contrastive learning objective guided by SAM masks. The resulting feature space is semantically coherent and well-separated, and final object-level segmentation is obtained via unsupervised clustering. This enables fast editing, such as object removal, composition, and style transfer, by directly manipulating the scene’s Gaussians. We evaluate TRASE on five dynamic benchmarks, demonstrating state-of-the-art segmentation performance from unseen viewpoints and its effectiveness across various interactive editing tasks. Our project page is available at: <https://yunjinli.github.io/project-sadg/>

1. Introduction

Humans experience the world in motion, where objects persist over time despite changes in pose, shape, and appearance. Our ability to recognize objects remains stable, even as we move and observe them from different vantage points. This phenomenon suggests the existence of neural 3D representations, which preserve semantic consistency across

both space and time. Such representations are central for applications in augmented reality, gaming, and autonomous systems, where interactive manipulation of dynamic scenes requires object-level segmentation that is spatio-temporally consistent and efficient.

Neural Radiance Fields (NeRFs) [31] have significantly advanced 3D reconstruction by enabling photorealistic novel view synthesis, but their implicit nature makes them computationally too expensive for real-time interaction. Gaussian Splatting (3DGS) [20] has recently emerged as a powerful alternative, achieving real-time rendering with explicit and compact scene representations. Dynamic extensions of 3DGS [28, 52] allow faithful reconstruction of moving scenes, but they lack built-in object segmentation and rely purely on geometry and color. While several works have integrated semantic information into static 3D Gaussian representations [6, 53], they fail to handle motion, deformation, and viewpoint variation in dynamic scenes.

Only a handful of works have explored the unification of semantics and dynamics in 3DGS [19, 24]. SA4D [19] incorporates segmentation into dynamic Gaussian splatting, using video object trackers to match masks across views similar to Gaussian Grouping [53]. However, approaches using these trackers often suffer from identity switches, causing inconsistent segmentation in multi-view settings – particularly in the presence of occlusions, non-rigid deformations, or rapid motion, as shown in Fig. 3. DGD [24] addresses temporal consistency by distilling semantically-aware features from foundation models like CLIP [45] and DINOv2 [32], enabling tracking. Yet, these features are high-dimensional, leading to significant computational

[†]Corresponding author. ^{*} Equal contribution.

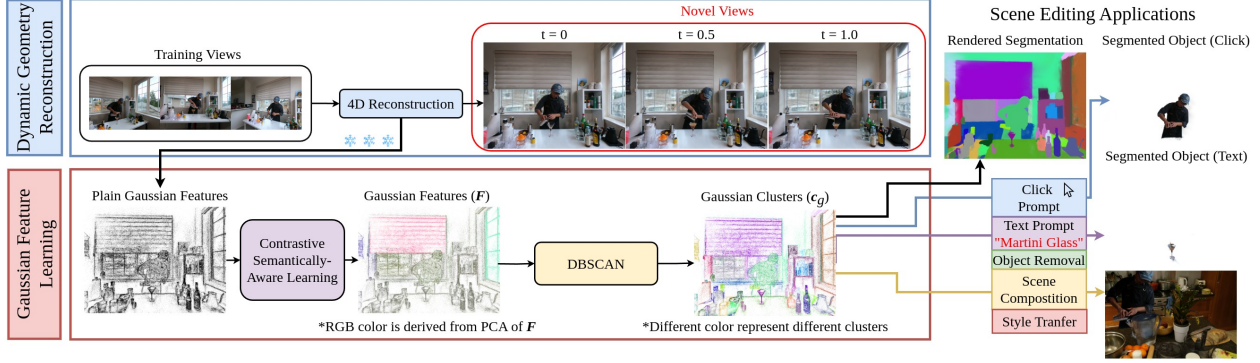


Figure 2. Our pipeline. TRASE consists of two main components: dynamic geometry reconstruction (Sec. 3.1) and Gaussian feature learning (Sec. 3.2). We adopt the approach from [52] to effectively learn dynamic 3D reconstruction. Given a 4D reconstruction, we learn Gaussian features $\mathbf{F} \in \mathbb{R}^{N \times 32}$ using a novel contrastive learning objective guided by SAM [22] masks. Once trained, we apply clustering [11] directly to the learned features, enabling segmentation field rendering. Our representation supports various scene-editing applications, including object segmentation via click/text prompts in our GUI, object removal, and scene composition.

overhead from both the large memory requirements and slow training.

In this work, we present TRASE, a tracking-free segmentation framework for dynamic scene understanding. TRASE learns temporally consistent segmentation features in a contrastive setting using only 2D binary masks. Unlike prior contrastive segmentation methods [12, 13, 54], which explicitly enforce cluster formation during training and promote statistical consistency of features, TRASE applies contrastive learning directly at the pixel-pair level in a fine-grained rendered feature space, deferring object clustering to a final post-training step. This design enables TRASE to learn a segmentation field with both high temporal consistency and sharp, well-defined object boundaries. It also effectively mitigates common artifacts, such as floaters and out-of-FoV errors, that frequently degrade prior contrastive learning approaches.

To the best of our knowledge, we are the first to introduce a benchmark for segmentation in novel views of dynamic scenes. While established datasets like DAVIS [3, 4, 35, 36] and VOS [47, 50, 51] address dynamic video segmentation, none evaluate segmentation quality in unseen viewpoints. Moreover, our benchmark is significantly larger than the evaluation protocol suggested in [24], as our test sequences comprise single- and multi-view scenes and captures real-world scenarios. Beyond achieving state-of-the-art segmentation accuracy, TRASE is tailored for real-time interactive scene editing. Our compact 32-dimensional feature space requires minimal post-processing and integrates seamlessly into object manipulation tasks such as style transfer, recoloring, composition, and removal.

Our contributions can be summarized as follows:

- We propose TRASE, a new approach for multi-view consistent segmentation of dynamic scenes without tracking labels. To achieve this, we design a novel contrastive

learning objective based on differentiable feature rendering and contrastive learning, ensuring segmentation stability across time and views.

- We offer a broad benchmark for segmentation in novel views of dynamic scenes, which encompass a broad spectrum of camera setups and captured scenarios.
- We extensively evaluate our method on five dynamic datasets and achieve state-of-the-art segmentation performance in both single- and multi-view settings.
- We demonstrate the applicability of our feature space to several scene editing tasks, including object removal, style transfer, and scene composition.

2. Related Works

2.1. 3D Segmentation

In static scenes. With the emergence of various vision foundation models, such as Segment Anything Model (SAM) [22], DINO [5], and DINOv2 [32], researchers start to integrate the semantics from these foundation models into their reconstruction. SA3D [7] is the pioneering method that extends 2D SAM masks across images into 3D consistent object masks. GARField [21] introduces hierarchical grouping, leveraging the physical scales of 2D masks to group objects of different sizes and represent scenes at different granularity scales. Gaussian Grouping [53] first proposes to utilize consistent object IDs generated by video tracker DEVA [8] to render object IDs into camera views. Concurrent work such as SAGA [6] utilizes the masks generated from SAM, combined with scales obtained from 3D data inspired by GARField, to segment objects of various sizes. GAGA [29] proposes a mask group identity assignment technique using a 3D-aware memory bank to compensate for inaccurate semantic labels and use group IDs as pseudo-labels for identity encoding. Our model implicitly

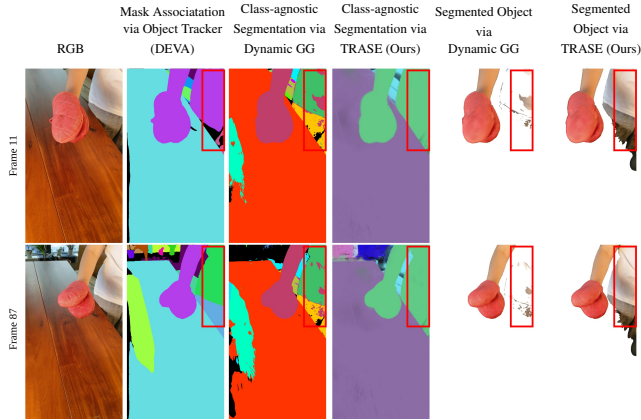


Figure 3. Example of a failure case from the video tracker DEVA [8]. Different colors refer to various object IDs associated by the model. We can observe that due to the inconsistent presence of the human torso in the video, DEVA fails to provide reliable and consistent object masks for supervision, resulting in a noisy class-agnostic segmentation and poorly segmented objects for dynamic Gaussian Grouping [53] (GG). We also provide a video of this example in the supplementary materials.

learns multi-view consistent semantic Gaussian features using our designed contrastive loss in a single training stage without identity assignments.

In dynamic scenes. To the best of our knowledge, only two prior works, SA4D [19], and DGD [24], address the segmentation task in dynamic 3DGS. DGD extends the rasterization pipeline of 3DGS to be able to render the semantic features of each Gaussian. The rendered Gaussian feature map is then trained with the supervision of DINOv2 [32] or CLIP [37] to mimic the output from their feature extractors. The drawbacks of such supervision are longer training times and bigger 3DGS models, as the dimensions of the features generated by DINOv2 and CLIP are quite large (384 and 512), and the Gaussian features are also stored. Following the identity encoding concept from Gaussian Grouping and its derivatives [10, 29], SA4D introduces a temporal identity feature field. As the method relies on consistent object IDs for supervision, it is sensitive to temporal tracking inaccuracies due to occlusion or fast motion. A concurrent work, Split4D [17], follows several proposed design choices, including single-frame supervision and a contrastive learning objective, and utilizes a recent 4D reconstruction model to achieve 4D segmentation. Our TRASE does not rely on tracking labels and effectively handles single- and multi-view data with fast rendering times, minimal post-processing, and low memory footprint.

2.2. Contrastive Learning for 3D Segmentation

A number of recent works define multi-view 3D segmentation as a contrastive learning objective. Contrastive Gaussian Clustering (CGC) [12] training aims to maximize intra-cluster similarity in the 2D rendered feature space by en-

forcing the feature’s proximity with its corresponding cluster’s mean feature and ensuring its spatial consistency. OmniSeg3D [54] follows a similar CGC objective and supervises 3D point clustering using SAM-based image patches. ContrastiveLift [13] proposes a slow-fast contrastive fusion strategy, where a slow network aggregates global object-level information while a fast network refines per-point features. OpenGaussian [46] enforces intra-cluster similarity and inter-cluster dissimilarity of rendered features and further trains their discretized version. Split4D [17] utilizes the same objective as [12] and additionally enforces the features to align with DINOv2 [32] in the early training stage. Our TRASE proposes a contrastive objective based on soft sample mining of pixel pairs, which focuses on only imperfect features and allows us to learn the segmentation field effectively in 4D. No costly distillation is required as we supervise the training with binary 2D masks.

2.3. Scene Editing Applications

Learning a semantically aware latent space enables interactive scene editing at the object level. Existing radiance-field editing methods are either restricted to single objects [16, 45] or rely on per-object scene decompositions [23, 49], which limit editing to a fixed set of instances. Other approaches, such as DINO [32], distill features into volumetric fields [44], but their implicit representations require expensive re-rendering for consistency, hindering real-time interaction. Gaussian-based methods [20] alleviate NeRF runtime issues via explicit point-based primitives: SAGA [53] enables local Gaussian editing, and Feature3DGS [56] leverages 2D foundation models like SAM [38] and LSeg [25] for promptable, language-guided 3D edits, yet all focus on static scenes. In contrast, our method edits dynamic objects with temporally consistent results and supports diverse tasks, including style transfer, object removal, and composition [24]. While SA4D [19] offers semantic scene editing, it requires prior object labels and limited interaction. In contrast, our framework provides a user-friendly graphical interface that supports simple text prompts and mouse-based selection.

3. Method

In this section, we introduce our novel TRASE. As illustrated in Fig. 2, the pipeline comprises two main components: dynamic geometry reconstruction (Sec. 3.1) and Gaussian feature learning (Sec. 3.2). We adopt the Deformable-3DGS [52] pipeline to reconstruct the 4D scene. Once the 4D reconstruction is learned, we freeze this representation and proceed with Gaussian feature learning using SAM [22] masks and our novel contrastive learning objective in the rendered feature space.

3.1. Dynamic Geometry Reconstruction

We follow the approach proposed in [52] and describe it briefly for completeness. Unlike Dynamic3DGS [28] model, where the reconstruction is stored per frame, resulting in high memory consumption, an MLP learns per-Gaussian deformation ($\delta\mathbf{x}_i, \delta\mathbf{r}_i, \delta\mathbf{s}_i$) with respect to the static canonical space \mathcal{G}_c , which is defined as $\mathcal{G}_c = \{\mathbf{x}_i \in \mathbb{R}^3, \mathbf{r}_i \in \mathbb{R}^4, \mathbf{s}_i \in \mathbb{R}^3, \alpha_i \in \mathbb{R}, \mathbf{sh}_i \in \mathbb{R}^{3 \times (D_{max}+1)^2}\}$ for $i = 1, \dots, N$. \mathbf{x}_i is the center position of the i -th Gaussian, \mathbf{r}_i is the quaternion representing the rotation, \mathbf{s}_i is the scaling vector, α_i refers to the opacity, and \mathbf{sh}_i is the Spherical Harmonic Coefficients encoding the color information ($D_{max} = 3$) as per [52].

The resulting Gaussians \mathcal{G}_t at timestamp t are defined as

$$\mathcal{G}_t = \{\mathbf{x}_i + \delta\mathbf{x}_i, \mathbf{r}_i + \delta\mathbf{r}_i, \mathbf{s}_i + \delta\mathbf{s}_i, \alpha_i, \mathbf{sh}_i\}_{i=1, \dots, N}. \quad (1)$$

Once \mathcal{G}_t is obtained, we proceed with the standard rasterization pipeline [20] to render the image \mathbf{I}_r . The color loss \mathcal{L}_{color} is computed with the ground truth image \mathbf{I}_{GT} as

$$\mathcal{L}_{color} = (1 - \lambda)\mathcal{L}_1(\mathbf{I}_{GT}, \mathbf{I}_r) + \lambda\mathcal{L}_{D-SSIM}(\mathbf{I}_{GT}, \mathbf{I}_r), \quad (2)$$

where λ refers to the weighting parameter for the structural similarity loss term.

3.2. Gaussian Feature Learning

Summary. Our feature learning augments each 3D Gaussian with a 32-dimensional feature vector, enabling segmentation without explicit tracking labels. It is worth noting that, in contrast to view-dependent spherical encoding, our semantic feature vector is consistent across different views and time. Thanks to differentiable feature rendering [56] and SAM [22] masks, we construct and explicitly enforce pixel-mask associations in the Gaussian feature field. Our novel contrastive learning objective is designed to be efficient by sub-sampling and effective by integrating SAM [22] masks. Using only 2D guidance and without any object labels, Gaussians are trained to separate per-pixel rendered features from different segments and align those within the same segment. To achieve this, we design a soft-mining objective. Unlike hard mining, which selects pairs strictly by similarity, soft mining uses a relaxed, existential rule that increases pixel coverage and makes training less sensitive to noisy feature similarities. Finally, the learned features are globally clustered, producing multi-view consistent segmentation.

Our notation. A generated set of SAM masks \mathcal{M}_{SAM} comprise M' binary masks of a given image \mathbf{I}_{GT} , where each mask M_i corresponds to a different segment. With this, we define the pixel-mask correspondence vector \mathbf{y}_i , which captures information across all binary masks in \mathcal{M}_{SAM} for a certain pixel coordinate (u_i, v_i) . This vector is similar to a one-hot encoding technique; however, there is no guarantee

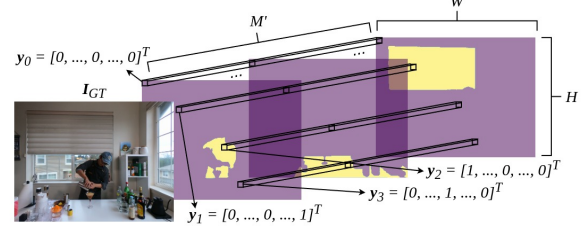


Figure 4. The illustration of pixel-mask correspondence vector \mathbf{y}_i . The pixel-mask correspondence vector is constructed from a subset of SAM masks \mathcal{M}_{SAM} for a given image \mathbf{I}_{GT} .

that a pixel belongs to a single mask due to 2D segmentation inaccuracies. We visually demonstrate the formulation of \mathbf{y}_i in Fig. 4.

The similarities of pixel-mask vectors for a pair of pixels (i, j) can be retrieved by computing the Gram matrix of their stacked matrix $\mathbf{Y} \in \{0, 1\}^{N_p \times M'}$, where N_p refers to the number of sampled pixels. All entries of the resulting Gram matrix are then bounded to either 0 (negative pair) or 1 (positive pair) to form a mask-based correspondence matrix $\mathbf{C} \in \{0, 1\}^{N_p \times N_p}$ among sampled pixels, formally defined as

$$\mathbf{C}(i, j) = \begin{cases} 1, & \text{if } \mathbf{y}_i^T \cdot \mathbf{y}_j > 0 \\ 0, & \text{otherwise.} \end{cases} \quad (3)$$

Analogous to the binary mask-based Gram matrix \mathbf{C} , we compute a feature-based matrix \mathbf{C}_F , capturing the pairwise similarities between the rendered features $\{\mathbf{I}_F(u_i, v_i)\}_{i=1, \dots, N_p}$. Following common practices [6], we consider a smooth version of Gaussian features, as it is more robust than considering individual features, which might have high similarity scores corresponding to unrelated objects. The smooth Gaussian feature is computed as the mean feature of its K nearest neighbors [9] based on the Gaussian's 3D position.

Our learning objective. To robustly learn multi-view coherent feature embeddings, we adopt a soft-mined contrastive learning objective. Unlike standard hard mining, which selects positive or negative pairs strictly based on their individual similarity values, soft mining employs an existential criterion: a positive pixel pair (i, j) is considered into final positive loss computation \mathcal{L}_{pos} if there exists any positive pair involving i whose similarity falls below the positive threshold τ_p . Similarly, a pair is included in the negative loss if there exists any negative pair involving i whose similarity exceeds the negative threshold τ_n . By design, the soft-mined strategy broadens pixel coverage during training, in contrast to naive hard sampling that typically concentrates on a sparse set of imperfect pixel pairs and leaves many pairs untrained. We further restrict the selection to non-redundant pairs by considering only the upper-triangular portion of the matrices ($i < j$). Formally, the

soft-mined masks are defined as

$$\mathbf{M}_{ij}^+ = (\exists k : \mathbf{C}_{ik} = 1 \wedge \mathbf{C}_{\mathbf{F},ik} < \tau_p) \wedge (i < j), \quad (4)$$

$$\mathbf{M}_{ij}^- = (\exists k : \mathbf{C}_{ik} = 0 \wedge \mathbf{C}_{\mathbf{F},ik} > \tau_n) \wedge (i < j). \quad (5)$$

The positive and negative losses are then computed as weighted sums over these masks:

$$\mathcal{L}_{\text{pos}} = -\frac{1}{Z} \sum_{i,j} \mathbf{M}_{ij}^+ \mathbf{W}_{ij} \mathbf{C}_{\mathbf{F},ij}, \quad (6)$$

$$\mathcal{L}_{\text{neg}} = \frac{1}{Z} \sum_{i,j} \mathbf{M}_{ij}^- \mathbf{W}_{ij} \text{ReLU}(\mathbf{C}_{\mathbf{F},ij}), \quad (7)$$

where Z is a normalization factor (e.g., the total number of pixel pairs), $\mathbf{W} \in \mathbb{R}^{N_p \times N_p}$ is a pixel-weight matrix similar to [6], and $\text{ReLU}(\cdot)$ ensures that only positive contributions are considered for negative pairs. The final loss is then defined in Eq. (8) with an extra regularization term to stabilize the feature learning.

$$\mathcal{L} = \mathcal{L}_{\text{pos}} + \mathcal{L}_{\text{neg}} + \mathcal{L}_{\text{reg}}, \quad (8)$$

$$\mathcal{L}_{\text{reg}} = \left(1 - \frac{1}{HW} \sum_{i=1}^{HW} \|\mathbf{I}_F(u_i, v_i)\|_2 \right)^2 \quad (9)$$

Inference. To enable interactive applications with the learned 4D representation, we deploy DBSCAN algorithm [11] to cluster the Gaussian features into several groups and generate the so-called Gaussian clusters. In contrast to the K-Means algorithm [27, 30], it does not require any prior knowledge of the number of clusters in a scene. As can be seen in Fig. 2, clusters represent distinct objects, which verifies accurate alignment of our learned feature space with the object-level semantic field.

We further observe that the object boundaries can be effectively refined by applying a simple similarity threshold, which prunes Gaussians with features that are less similar to the corresponding cluster's mean. This simple technique enhances the method's performance in challenging segmentation scenarios, such as those involving occlusions and affected by sparse observations.

4. Experimental Results

We first provide details of our proposed 4D segmentation benchmark in Sec. 4.1 and outline the evaluation protocol in Sec. 4.2. We present segmentation results of our model, along with both quantitative and qualitative comparisons to other related works [6, 24, 53] in Sec. 4.3. Last but not least, we demonstrate the capabilities of our learned semantic representation on a number of downstream tasks, including scene editing and selection via our designed graphical user interface (Sec. 6). Please refer to the supplementary material for implementation details.

4.1. 4D Segmentation Benchmark

We manually annotate dynamic sequences of existing novel-view synthesis datasets and present their segmentation-aware versions: *NeRF-DS-Mask*, *HyperNeRF-Mask*, *Neu3D-Mask*, *Immersive-Mask*, and *Technicolor-Mask*. Utilizing the powerful SAM2 model [38], which provides consistent object masks across video sequences, we define the objects of interest for each sequence to evaluate their segmentation performance in our model and manually refine them. Qualitative examples of the augmented sequences, together with a description of the raw datasets, can be found in the supplementary material.

4.2. Evaluation Protocol and Baselines

We compare our model with SAGA [6], Gaussian Grouping (GG) [53], SA4D [19], and DGD [24]. Additionally, we add evaluation with the contrastive learning methods such as Contrastive Gaussian Clustering (CGC) [12] and OpenGaussian [46]. Note that SAGA, Gaussian Grouping, CGC, and OpenGaussian are designed for static scenes and do not include a module to encode temporal information. To evaluate them on the 4D segmentation task, we integrate our 4D reconstruction backbone into their pipeline, extending their approach to effectively handle dynamic scenes. GG and SA4D require video object tracking labels for their supervision. To enable evaluation of the multi-view sequences from our benchmarks, we train the models on the camera closest to the test view (cam5 for Neu3D, cam2 for Immersive, and cam1 for Technicolor). After training, we manually perform click prompts in the rendered novel views of each scene trained by different approaches to select the objects of interest defined in the benchmark. Apart from the quantitative results, we also present qualitative results from various benchmarks, as certain insights cannot be fully captured through numerical evaluations alone. Following common practices, we use Mean Intersection over Union (mIoU) and Mean Pixel Accuracy (mAcc) to quantitatively evaluate the performance of the models.

4.3. Segmentation Results

As shown in Tab. 1, TRASE achieves state-of-the-art performance across all benchmarks, surpassing other segmentation methods. Please refer to the supplementary material for details on each sequence of the benchmark. Further, we select some sequences to illustrate the quality of the segmentation of each model in Fig. 5. These comparisons reveal that TRASE qualitatively surpasses existing models and exhibits multi-view consistent segmentation performance. Notably, TRASE maintains strong segmentation consistency to test camera views in multi-view sequences such as *flame_stea*, *Painter*, and *11_Alexa_2*. This robust performance can be attributed to the compact Gaussian features learned through the proposed Gaussian feature

Method	NeRF-DS-Mask		HyperNeRF-Mask		Neu3D-Mask		Immersive-Mask		Technicolor-Mask	
	mIoU↑	mAcc↑	mIoU↑	mAcc↑	mIoU↑	mAcc↑	mIoU↑	mAcc↑	mIoU↑	mAcc↑
GG [53]	0.8351	0.9729	0.8341	0.9771	0.8864*	0.9932*	0.7673*	0.9776*	0.7979*	0.9800*
SAGA [6]	0.8072	0.9644	0.7660	0.9579	0.6941	0.9516	0.7395	0.9747	0.7913	0.9792
DGD [24]	0.7125	0.9551	0.8297	0.9777	0.7721	0.9851	0.7981	0.9850	0.7791	0.9728
SA4D [19]	0.6740	0.9360	0.7371	0.9616	0.8832*	0.9391*	0.7987*	0.9835*	0.8271*	0.9734*
CGC [42]	0.8100	0.9718	0.8157	0.9768	0.8754	0.9927	0.8856	0.9925	0.8806	0.9812
OpenGaussian [46]	0.6939	0.9564	0.6311	0.9411	0.8178	0.9899	0.7120	0.9793	0.8390	0.9694
TRASE (Ours)	0.8768	0.9831	0.8663	0.9845	0.9022	0.9945	0.9234	0.9945	0.9308	0.9917

Table 1. Segmentation accuracy of 4D segmentation methods on our benchmark. TRASE outperforms the baselines on average mIoU and mAcc. The quantitative results for each sequence can be found in the supplementary. *: GG and SA4D need consistent object IDs from a video tracker for supervision [8]. To evaluate on the multi-view camera dataset, we train models on a camera closest to the test view.

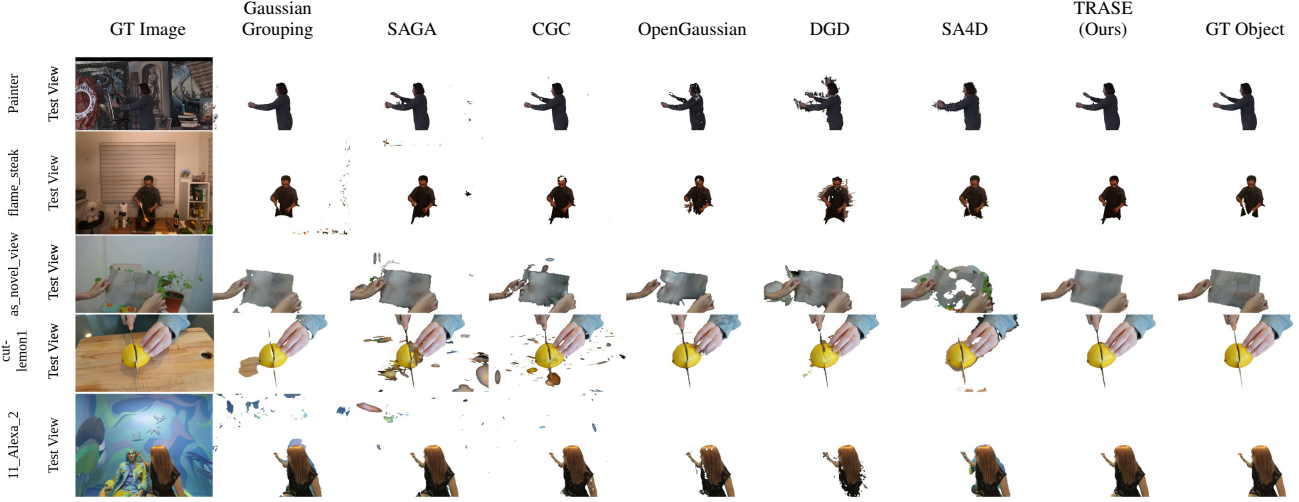


Figure 5. Segmentation qualitative results. While Gaussian Grouping [53] and SAGA [6] suffer from spurious Gaussians, our method demonstrates crisp and floater-free segmentation. Object boundaries in SA4D [19] and DGD [24] segmentations are not tight and capture part of the background while rendering. OpenGaussian [46] is not able to fully capture the whole objects in its segmentation. Our model consistently demonstrates superior segmentation quality and crisp object masks.

	Preproc	Training	Total (min)		Storage (MB)
DGD [24]	0.08	103	103		285
TRASE (Ours)	16	16	32		60

Table 2. Storage and time comparison between DGD [24] and TRASE on NeRF-DS [48]. TRASE achieves over 3× faster training time compared to DGD while only requiring 4.5× less memory in storage due to its compact Gaussian features.

training. In contrast, DGD segments objects by comparing cosine similarity scores between features retrieved via click prompts. However, determining a suitable threshold that generalizes across various scenes is neither straightforward nor intuitive. TRASE employs clustering based on the Gaussian features to group the Gaussians into several segments. As this operation is done in 3D space, TRASE achieves cross-view consistency and doesn't need to associate objects from different views. This advantage is evident in *cut-lemon1* example in Fig. 5, where wrongly associated object IDs can cause segmentation failure for [53].

5. Ablation Studies

5.1. Time and Storage Analysis

We perform a comprehensive time and storage analysis of TRASE and DGD [24] using an RTX 3080 and an Intel i7-12700 on the NeRF-DS [48] dataset. The results are shown in Tab. 2, where “Pre-Proc” refers to the generation of DINOv2 384-dim features for DGD and SAM masks for TRASE. Rendering 384-dim features into 2D is computationally inefficient, significantly slowing down DGD’s training process. TRASE uses 32-dim Gaussian features, which can be rendered much more efficiently. As a result, TRASE achieves over 3× faster total time than DGD while only requiring 4.5× less space in storage.

5.2. Soft Sample Mining

We visually demonstrate the effectiveness of our soft-mined pixel-pair sampling strategy in comparison to other contrastive objectives: sampling all positive–negative pairs (all) and sampling only pairs that individually satisfy the thresh-

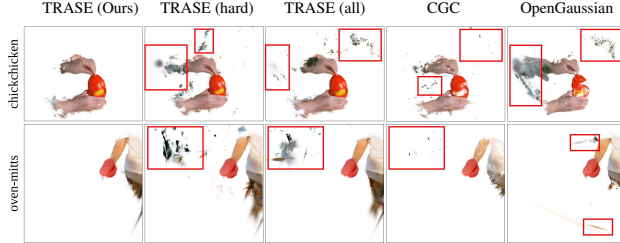


Figure 6. Qualitative results of segmented objects in *chickchicken* and *oven-mitts* sequence in out-of-FoV viewpoint. TRASE with soft sample mining (Ours) exhibits superior performance over TRASE with hard / all mining, CGC [12], and OpenGaussian [46].

Method	HyperNeRF-Mask		Immersive-Mask		Technicolor-Mask	
	mIoU↑	mAcc↑	mIoU↑	mAcc↑	mIoU↑	mAcc↑
TRASE (multi-frame)	0.8636	0.9833	0.8968	0.9933	0.9309	0.9913
TRASE (Ours)	0.8663	0.9845	0.9234	0.9945	0.9308	0.9917

Table 3. Ablation study on single-frame mask supervision. The multi-frame baseline propagates masks between consecutive frames using Gaussian motion flow to impose temporal constraints. While this increases training time by a factor of 2, it does not provide significant additional supervision, confirming the effectiveness of single-frame mask supervision.

olds (hard). We include contrastive-based baselines such as CGC [12] and OpenGaussian [46] for completeness. By investigating the out-of-FoV regions, i.e., 3D regions outside the observable space of train and test views, we observed floaters in the segmentation by our method without soft selection and other contrastive baselines, as shown in Fig. 6. Our mining approach effectively eliminates these floaters, leading to more stable and reliable segmentation. It is worth noting that no post-processing filtering is applied to ensure a fair comparison.

5.3. Single-frame Mask Supervision

Inspired by classical tracking methods [15] and recent work linking 3DGS dynamics to pixel motion [14], we investigate the impact of incorporating temporal constraints on our single-frame mask supervision. Specifically, we compare our standard single-frame approach with a temporal extension, where masks are propagated across consecutive frames to encourage segmentation consistency over time. To implement this, we estimate optical flow between consecutive training timestamps t_s and t_{s+1} using differentiable rendering with accumulated 2D Gaussian displacements [14], and warp mask pixels from t_s to t_{s+1} . Quantitative results are presented in Tab. 3. As observed, the multi-frame baseline does not provide significant improvements over the single-frame supervision, despite the doubled training cost, as an additional 2D flow and all associated parameters are rendered. This validates our design choice to rely on single-frame mask supervision, which achieves strong segmentation performance efficiently.

Method	Filtering	NeRF-DS-Mask		HyperNeRF-Mask		Neu3D-Mask	
		mIoU↑	mAcc↑	mIoU↑	mAcc↑	mIoU↑	mAcc↑
SAGA [6]	✗	0.8072	0.9644	0.7660	0.9579	0.6941	0.9516
TRASE	✓	0.8421	0.9778	0.8223	0.9779	0.8026	0.9853
TRASE (Ours)	✗	0.8760	0.9829	0.8368	0.9790	0.8738	0.9923
TRASE (Ours)	✓	0.8768	0.9831	0.8663	0.9845	0.9022	0.9945

Table 4. Effect of filtering spurious Gaussians for SAGA [6] and TRASE. Despite the improved baseline’s performance, TRASE maintains the superior segmentation quality due to its spatially consistent feature space.

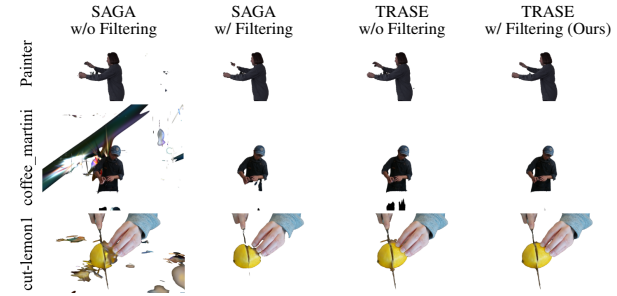


Figure 7. Qualitative results for SAGA [6] with (w/) and without (w/o) our proposed filtering. Even though our filtering step can filter most of the artifacts from SAGA, their resulting segmented objects are still not optimal compare to TRASE.

5.4. Post-processing Filtering

We provide an ablation study of our method with respect to the filtering step, which removes Gaussians whose features are too dissimilar to the object’s mean. As shown in Tab. 4, the proposed filtering step enhances the segmentation quality of our method. Particularly, artifacts on the object’s boundaries are effectively removed, mitigating the inaccuracies in input masks or the effects of occlusions.

We further demonstrate the advantage of our learned feature field by showing that while the post-processing step enhances segmentation accuracy, it is not the sole factor driving our superior performance. We also note that this technique is applicable only to certain baselines such as SAGA [6]. For example, methods like CGC [12] and DGD [24] already incorporate a similarity threshold during inference. OpenGaussian [46] gets the assigned class ID for each Gaussian from their codebook. By contrast, SA4D [19] and Gaussian Grouping [53] learn an identity field, making our post-processing inapplicable to them. In Tab. 4 and Fig. 7, we quantify and illustrate the effectiveness of applying our proposed filtering step to SAGA [6]. However, because the features learned under the baseline’s hard-contrastive objective remain suboptimal, the segmentation quality still exhibits more artifacts compared to TRASE.

6. Editing Applications

In addition to accurate segmentation capabilities and multi-view consistent rendered masks, we demonstrate the effectiveness of our learned semantic feature field in a range

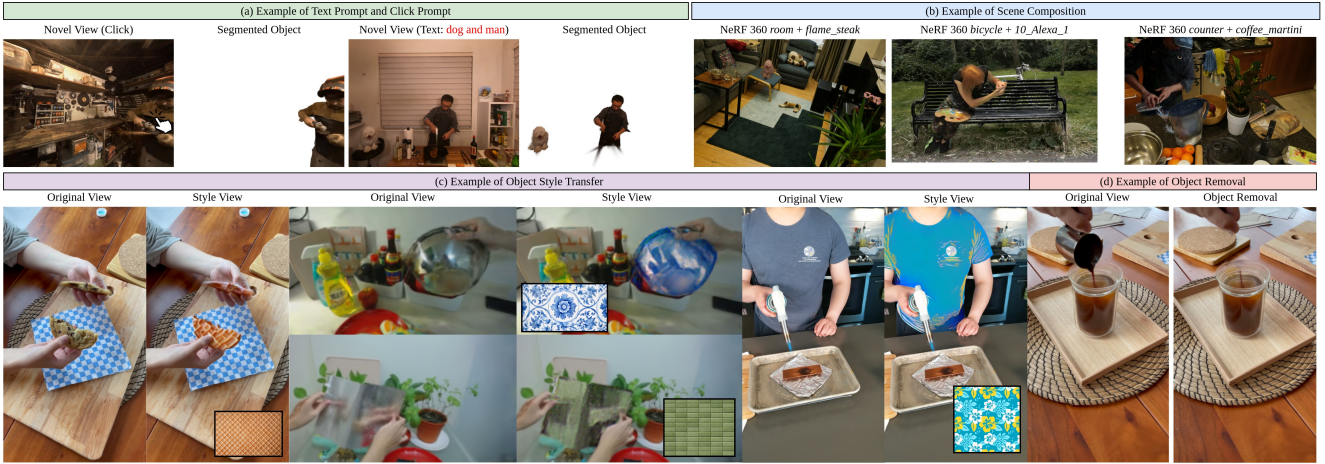


Figure 8. Versatile scene editing applications. (a) The object of interest can be selected by click prompts or text prompts. (b) Scene composition can be done by manipulating the selected Gaussians in another scene. (c) Style transfer of the segmented objects to obtain different textures. (d) Object removal for the selected object.

of downstream tasks. Specifically, we focus on interactive editing applications and develop a graphical user interface (GUI) to grant full user control over the representation. Thanks to its explicit nature and our semantic abstraction to Gaussian clusters, we achieve real-time operation capability in handling many editing tasks. We provide snapshots of the GUI in the supplementary.

In addition to simple click prompts, we also support text-based prompts to make object selection even more intuitive. To enhance 3D content editing in dynamic scenes, we integrate style transfer capabilities for the selected objects. By segmenting objects directly in 3D, we facilitate scene composition and object removal through straightforward manipulation of the selected Gaussians. Due to the space limit, we shall provide more qualitative results in the supplementary. In the following, we describe the implementation details of editing tasks based on our semantically-aware feature field.

Text Prompt. Inspired by Gaussian Grouping [53], we employ Grounded SAM [39] to generate a 2D mask based on the text prompt in the novel view. The 2D mask is re-projected into the 3D space with the rendered depth information. Finally, we associate each reprojected point with its nearest Gaussian in the 3D scene and retrieve its corresponding cluster. If the number of associated Gaussians of a given cluster is more than a threshold, the cluster would be selected. The example of text prompts on different sequences is shown in Fig. 8 (a).

Scene Composition. We also perform qualitative results on scene composition. As the segmentation is performed in 3D, we can simply put the selected Gaussians from the dynamic scene into another static or dynamic scene. The scales and coordinate transformation need to be adapted. We show some examples of scene composition in Fig. 8.

Object Style Transfer. We adopt the static Gaussian style

transfer from StyleSplat [18] for dynamic scenes. Given a rendered image I_r and a style image I_s , we extract their feature maps (F_r, F_s respectively) from VGG16 [43] and optimize only the SHs of the Gaussians of the selected cluster with the nearest-neighbor feature matching (NNFM) loss [55]. Fig. 8 (c) illustrates an example of style transfer on the segmented object.

Object Removal. We can also remove objects by simply deleting Gaussians belonging to the specific cluster as illustrated in Fig. 8 (d). It is worth noting that an additional inpainting step may be required, where the newly exposed parts have not been learned from multi-view observations.

7. Conclusion

We introduced a novel framework for dynamic scene understanding, which enables multi-view consistent segmentation without any object tracking supervision. Our TRASE effectively combines dynamic 3D Gaussian Splatting 3DGS [52] and 2D SAM [22] masks in a contrastive learning objective, which lifts semantic information into 3D space and learns expressive Gaussian features based on soft sample mining. This results in cross-view consistency when rendering segmented objects, enhancing the quality and coherence of object segmentation across different views. Evaluated on various novel-view datasets, TRASE shows superior performance both quantitatively and qualitatively. We further demonstrate the effectiveness of the learned feature field on downstream editing tasks such as point and text prompts, style transfer, object removal, and scene composition. Our approach sets a strong foundation for further research into dynamic scene understanding and scene editing, especially in complex multiview scenarios. We intend to release our code and benchmarks for future developments.

TRASE: Tracking-free 4D Segmentation and Editing

Supplementary Material

In the supplementary, we provide several examples from our segmentation benchmark, along with dataset details (Sec. 8). Further implementation details are described in Sec. 9 and Sec. 10. A range of ablation studies on different components of our pipeline is given in Sec. 11. In Sec. 12 we address several limitations of our method and potential directions for future work. We provide additional visualizations of our learned feature space in comparison to other contrastive-based segmentation methods in Sec. 13 and Sec. 14. In Sec. 15 we show more examples on how our soft mining successfully mitigates floaters. Further, we present detailed quantitative results on all benchmarks in Sec. 17. We finally demonstrate qualitative results of our method on segmentation (Sec. 18, Sec. 19) and editing (Sec. 16).

8. Segmentation Benchmark

As discussed in Sec. 4.1 (main), we employ SAM2 [38] to manually select objects of interest to form our segmentation benchmarks for dynamic scene novel view synthesis. The examples are illustrated in Fig. 9. We describe the details of the mask storage for training and datasets adapted for our segmentation benchmark in the following.

Mask Storage. We employ SAM [22] to generate the anything-masks for Gaussian feature learning. However, the resulting masks are memory-inefficient because they are stored in a dense format ($M \times W \times H$) with a lot of zero-pixels. To optimize memory usage, we save the masks as a bit array. Given a permuted tensor version of an RGB image $I \in \mathbb{R}^{3 \times W \times H}$, SAM generates masks $\mathcal{M} \in \mathbb{R}^{M \times W \times H}$. We first flatten \mathcal{M} , then convert flattened ($M \times W \times H$)-dimensional array into a bit-array. The final output is stored in a dictionary with the required information to re-create the original mask tensor: a number of masks M , image dimensions (W, H) , and the compressed bit array, i.e., M, W, H , bitarray. This approach significantly reduces the storage used and is particularly useful for multi-view datasets, where numerous masks from different views are generated. For instance, a raw mask generated from an image in *coffee_martini* occupies around **80 MB**, but the dictionary representation reduces to about **1 MB**.

NeRF-DS. [48] contains scenes with challenging transparent and shiny moving objects recorded by two monocular cameras. Five sequences are used for reconstruction and evaluation including *as_novel_view*, *basin_novel_view*, *cup_novel_view*, *press_novel_view*, and *plate_novel_view*.

HyperNeRF. [33] is recorded using a single monocular camera. The camera moves while capturing the dynamic

scenes involving different human-object interactions. In our experiments, we use ten sequences: *americano*, *split-cookie*, *oven-mitts*, *espresso*, *chickchicken*, *hand1-dense-v2*, *torchocolate*, *slice-banana*, *keyboard*, and *cut-lemon1*.

Neu3D. [26] contains videos captured by a multi-view rig with 18 to 21 cameras each at 30 FPS. The scenes involve a person performing cooking tasks in the kitchen. In total, five scenes are used in our experiments: *coffee_martini*, *cook_spinach*, *cut_roasted_beef*, *flame_steak*, and *sear_steak*.

Google Immersive. [2] consists of videos captured by a 46-camera rig at 30 FPS. The cameras are fish-eye cameras and are distributed on the surface of a hemispherical, 92cm diameter dome. Four scenes are used in our experiments: *01_Welder*, *02_Flames*, *10_Alexa_1*, and *11_Alexa_2*.

Technicolor Light Field. [40] captures scenes using a 4×4 camera array at 30 FPS. We use the undistorted images provided by the authors, and four scenes are used in our experiments: *Birthday*, *Fabien*, *Painter*, and *Theater*.

9. Training Implementation Details

We implement the whole pipeline in PyTorch [34]. We reuse the codebase from Deformable-3DGS [52] and extend the differential Gaussian rasterization pipeline to render the Gaussian features similar to [53]. In the following sections, we present the detailed training and evaluation setup for various datasets.

9.1. NeRF-DS and HyperNeRF

For the NeRF-DS sequences, we use the left camera for training and the right camera for testing. In the HyperNeRF sequences, training frames are sampled every 4 frames, starting from the first frame, while testing frames are selected every 4 frames, starting from the third frame. This follows the interp-sequence data-loading pipeline from the original HyperNeRF paper [33], ensuring that all testing frames are unseen during training. Note that we use 2x-downsized images for all experiments.

Dynamic Geometry Reconstruction. We adopt the default hyper-parameters from Deformable-3DGS [52]. Initially, the Gaussians are warmed up without the deformation MLP for the first 3k iterations to better capture the positions and shape stably as suggested in [52], after which the MLP optimization begins, and the 3D Gaussian and the deformation MLP are trained jointly. The densification of Gaussians for adaptive density control introduced in 3DGS [20] is set to run until 15k iterations. The dynamic geometry reconstruction is trained for a total of 20k iterations.

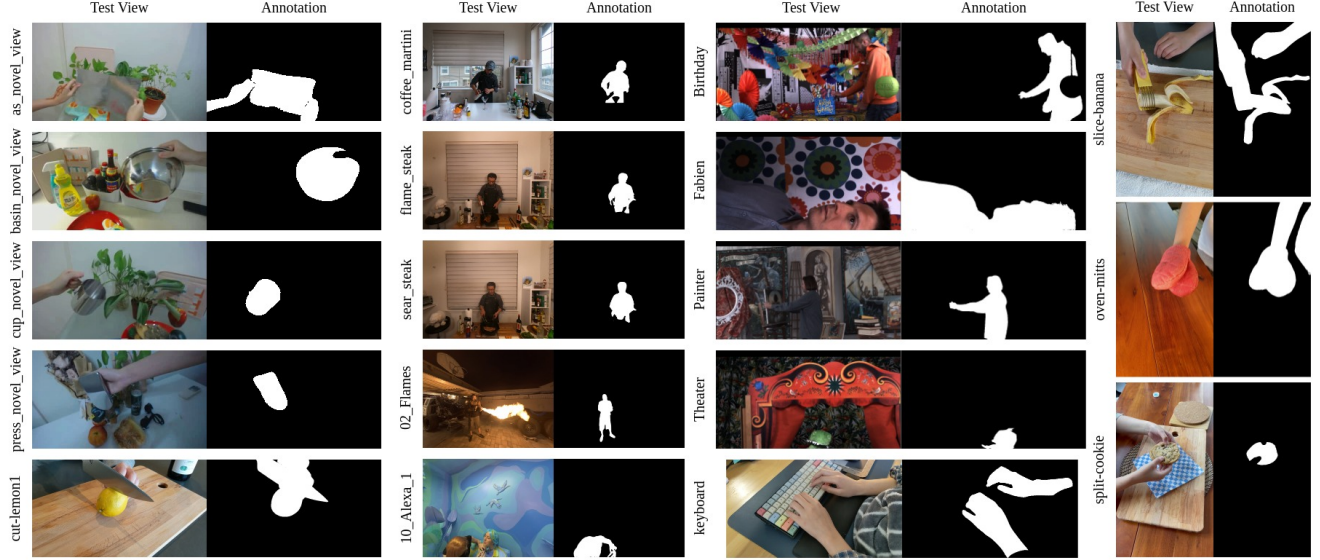


Figure 9. Image-object mask examples from our proposed extension to existing NVS datasets for dynamic 4D segmentation and downstream editing tasks. We ensure multi-view and temporal consistencies of the masks.

Method	NeRF-DS-Mask		HyperNeRF-Mask		Neu3D-Mask		Immersive-Mask		Technicolor-Mask	
	mIoU	mAcc	mIoU	mAcc	mIoU	mAcc	mIoU	mAcc	mIoU	mAcc
TRASE (K=0)	0.8228	0.9706	0.8360	0.9787	0.8661	0.9920	0.8725	0.9909	0.9259	0.9908
Ours (K=16)	0.8760	0.9829	0.8368	0.9790	0.8738	0.9923	0.9154	0.9942	0.9258	0.9904
TRASE (K=32)	0.8754	0.9828	0.8331	0.9780	0.8702	0.9922	0.9217	0.9944	0.9255	0.9904

Table 5. Comparison of average mIoU and mAcc per benchmark with K=0 (no smooth Gaussian features), K=16, and K=32. Our approach strikes a balance between performance and runtime requirements.

Gaussian Feature Learning. After the dynamic reconstruction is completed, we freeze model’s weights and begin Gaussian feature learning for an additional 10k iterations. For each image, we randomly sample 25 masks ($M' = 25$) generated by SAM [22] and 5k pixels ($N_p = 5000$), with K = 16 to get smooth Gaussian features.

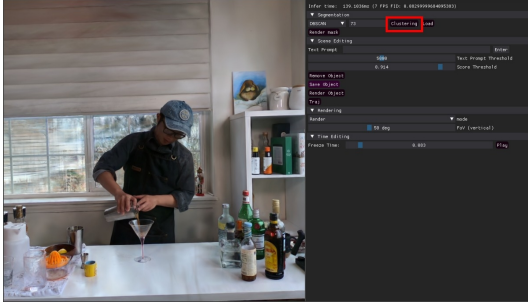


Figure 10. Example of our GUI operation. After opening the GUI, click “Clustering” to perform Gaussian feature clustering.

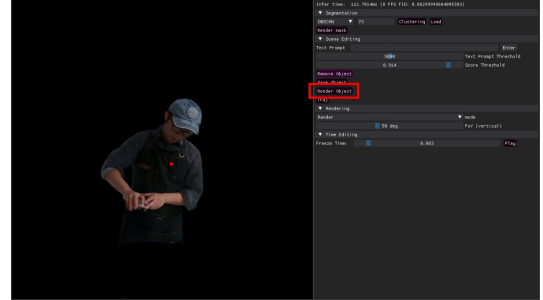


Figure 11. Example of our GUI operation. Hold the key “A” and click (red box) on the objects of interest in the novel view to segment the target objects.

9.2. Neu3D

Each video contains 300 frames, and we begin by downscaling the images by a factor of 2, resulting in a resolution of 1352×1014 . The center camera (camera_00) is used for testing, while the remaining cameras are for training. Initially, we run SfM [41] across all the first frames, excluding camera_00, to get the initial point cloud.

Dynamic Geometry Reconstruction. We follow the same

pipeline for dynamic geometry reconstruction as described in Sec. 9.1, except the densification of Gaussians is set to 8k iterations.

Gaussian Feature Learning. After the dynamic reconstruction is completed, we freeze the model’s weights and begin Gaussian feature learning for an additional 10k iterations. For each image, we randomly sample 50 masks ($M' = 50$) generated by SAM [22] and 10k pixels ($N_p = 10000$), with $K = 16$ to get the smooth Gaussian feature.

9.3. Google Immersive

Each video contains frames captured by fish-eye cameras with 300 frames. We first undistort the images and align the principal points to the center, then downscale them to a resolution of 1280×960 .

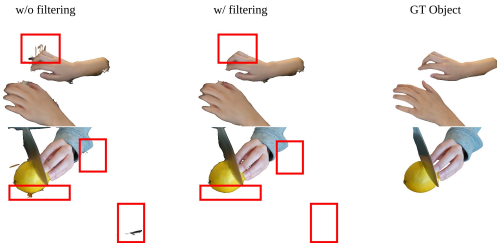


Figure 12. Visualization of ground-truth object of interest, segmented object without (w/o) filtering, and segmented object with (w/) filtering.

Similar to Neu3D, the center camera (camera_0001) is used for testing, while the other cameras are used for training. We generate the initial point cloud using SfM across all the first frames, excluding the test camera, and apply the same hyper-parameters as in Neu3D in Sec. 9.2.

9.4. Technicolor Light Field

We use the undistorted images provided by the authors, aligning the principal points to the center and resizing the images to a resolution of 1024×544 . Similar to Neu3D and Google Immersive dataset, the center camera (camera_0000) is used for testing, while the other cameras are used for training. We generate the initial point cloud using SfM across all the first frames excluding the test camera and apply the same hyper-parameters as in Neu3D in Sec. 9.2.

10. Testing Implementation Details

After the dynamic geometry reconstruction and Gaussian features are properly trained, we proceed to our GUI to select the object of interest and evaluate the model’s performance.

Given a clicked point $[u, v]^T$ on the novel view, we first use the known camera intrinsics to compute the inverse intrinsic matrix \mathbf{K}^{-1} . With the depth information d rendered

by the dynamic reconstruction of the Gaussians \mathcal{G}_t at time t , we can reproject the 2D clicked point to 3D coordinates in the camera frame. Finally, using the known camera extrinsics (rotation matrix \mathbf{R} and translation vector \mathbf{T}) for the world-to-camera transformation, we convert the points back into the world coordinate frame. We can then use this point coordinate to query its nearest neighbor Gaussian using KNN. The cluster ID corresponding to its nearest neighbor Gaussian is subsequently retrieved.

We provide interactive illustrations in our GUI to segment target objects as follows:

1. Open the GUI and run DBSCAN (Click button "Clustering") to group Gaussians into different clusters based on the learned Gaussian features as illustrated in Fig. 10.
2. Click the objects of interest in the novel view to segment the target objects as shown in Fig. 11.
3. Optional: Adjust the threshold to refine the object’s boundaries ($T_{\text{Neu3D}} = 0.98$, $T_{\text{NeRF-DS}} = 0.4$, $T_{\text{HyperNeRF}} = 0.9$, $T_{\text{Technicolor}} = 0.9$, $T_{\text{Immersive}} = 0.6$).
4. Click the button "Render Object" to render the selected object to test views for evaluating the performance.

11. Ablation Studies

11.1. Smooth Gaussian Features

As mentioned in Sec. 3.2, we utilize smooth versions of Gaussian features, which can be defined as follows:

$$\mathbf{f}_i^s = \frac{1}{K} \sum_{j \in \text{KNN}(i)} \mathbf{f}_j. \quad (10)$$

We provide a detailed analysis of the selection of the number of nearest neighbors for the KNN algorithm in Tab. 5. Overall, when smooth Gaussian features are enabled ($K = 16$ and $K = 32$), the performance is better than when smooth Gaussian features are disabled ($K = 0$). Since there is no significant improvement between $K = 16$ and $K = 32$, we eventually chose $K = 16$ for our pipeline to avoid additional overheads with the KNN sampling.

11.2. Gaussian Feature Clustering

We also employ a subsampling strategy to enable real-time Gaussian feature clustering in scenes that typically contain more than 300k Gaussians. We perform time analysis with different sub-sampling numbers of Gaussians (2%, 10%, and 25%) on RTX3080 and Intel i7-12700. For each scene, we compute the time for clustering using Python `timeit` package and take the average clustering time for five runs per scene. We report the average clustering time across all scenes in each benchmark and the corresponding mIoU and mAcc for our object of interest in Tab. 6. Overall, with different sub-sampling of Gaussians (2%, 10%, and 25%), the mIoU and mAcc stay almost unchanged. However, as

NeRF-DS-Mask				HyperNeRF-Mask				Neu3D-Mask				Immersive-Mask				Technicolor-Mask													
Avg. Num. Gaussians		186455.4		565614.7		678566		985713		457677.75		mIoU		mAcc		time↓		mIoU		mAcc		time↓		mIoU		mAcc		time↓	
Method	mIoU	mAcc	time↓	mIoU	mAcc	time↓	mIoU	mAcc	time↓	mIoU	mAcc	time↓	mIoU	mAcc	time↓	mIoU	mAcc	time↓	mIoU	mAcc	time↓	mIoU	mAcc	time↓	mIoU	mAcc	time↓		
*TRASE (2%)	0.8760	0.9829	0.4068	0.8368	0.9790	2.3117	0.8738	0.9923	2.2506	0.9154	0.9942	9.6083	0.9258	0.9904	1.6118														
TRASE (10%)	0.8707	0.9828	1.5782	0.8384	0.9794	11.8430	0.8792	0.9930	6.1878	0.9160	0.9939	71.2429	0.9283	0.9908	6.8211														
TRASE (25%)	0.8762	0.9832	3.9425	0.8461	0.9809	43.2682	0.8886	0.9935	18.8976	0.9180	0.9943	221.7642	0.9297	0.9907	19.0767														

Table 6. Comparison of average mIoU, mAcc, and clustering time per benchmark with different sub-sampling of Gaussians 2%, 10%, and 25%. *Our selection for our pipeline.

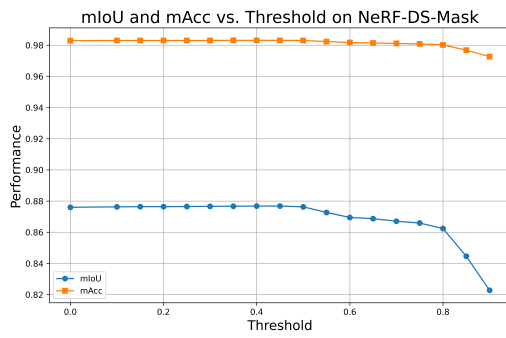


Figure 13. The sensitivity of TRASE with respect to the threshold selection for our post-processing filtering on NeRF-DS-Mask benchmark. Our model maintains accuracy across a wide range of threshold values, demonstrating the robustness and reliability of the learned feature field.

increasing the number of Gaussians results in a longer clustering time, we believe that 2% is the optimal sub-sampling number for clustering.

11.3. Sensitivity of Post-processing Filtering Threshold

We also evaluated the sensitivity of the post-processing filtering threshold. As illustrated in Fig. 13, there exists a wide margin of effective values. This demonstrates that selecting a threshold is not difficult, as one can easily choose a valid setting by observing the performance tendency.

11.4. DBSCAN vs. K-Means

There are various clustering techniques and K-means [27, 30] is one of the most widely used. K-means partitions data into k clusters, where each feature belongs to the cluster with the nearest centroid (mean of the cluster). The value k must be predefined, and the algorithm iteratively adjusts the centroids to minimize the sum of squared distances between features and their corresponding cluster centers. Therefore, the performance of the algorithm heavily depends on the optimal value of k .

To investigate this, we conducted an additional ablation study comparing the rendered segmentation produced by K-means with different values of k and DBSCAN. As shown in Fig. 14, the choice of k significantly impacts the result

Sampling rule	NeRF-DS-Mask		HyperNeRF-Mask		Neu3D-Mask	
	mIoU	mAcc	mIoU	mAcc	mIoU	mAcc
By Area	0.8403	0.9743	0.8171	0.9632	0.8679	0.9920
By Score	0.8028	0.9643	0.7998	0.9722	0.7673	0.9831
Grid-based	0.8721	0.9822	0.8484	0.9809	0.8708	0.9922
Random (Ours)	0.8768	0.9831	0.8663	0.9845	0.9022	0.9945

Table 7. Ablation study on mask sampling technique.

of rendered segmentation. Since different sequences contain varying numbers of objects, we believe that employing a method with an adaptive number of clusters, such as DBSCAN, validates our design choices with additional flexibility and no loss on the segmentation accuracy.

11.5. Gaussian Feature Dimension

We also analyze the impact of Gaussian feature dimensionality $D \in \{16, 32, 64, 128\}$ on segmentation performance. As shown in Tab. 8, increasing D does not lead to a clear improvement in mIoU or mAcc. On the other hand, the runtime costs such as storage requirements and clustering time increase significantly with larger D as shown in Tab. 9. Fig. 15 visualizes these trade-offs by plotting the no-filtered mIoU from HyperNeRF-Mask against runtime costs. Ideally, the optimal configuration should be located at the top-left corner (high mIoU, low cost). The plot confirms that our chosen dimensionality ($D = 32$) strikes the best balance between segmentation performance and computational efficiency.

D	Filtering	NeRF-DS-Mask		HyperNeRF-Mask		Neu3D-Mask	
		mIoU↑	mAcc↑	mIoU↑	mAcc↑	mIoU↑	mAcc↑
D=16	✗	0.8730	0.9822	0.8339	0.9778	0.8702	0.9921
	✓	0.8733	0.9822	0.8563	0.9828	0.9036	0.9945
D=32	✗	0.8760	0.9829	0.8368	0.9790	0.8738	0.9923
	✓ (Ours)	0.8768	0.9831	0.8663	0.9845	0.9022	0.9945
D=64	✗	0.8744	0.9825	0.8347	0.9780	0.8949	0.9939
	✓	0.8756	0.9830	0.8573	0.9832	0.9068	0.9948
D=128	✗	0.8752	0.9826	0.8320	0.9775	0.8936	0.9938
	✓	0.8761	0.9830	0.8573	0.9830	0.9070	0.9948

Table 8. Performance analysis of different dimensionality of Gaussian features ($D \in \{16, 32, 64, 128\}$).

11.6. Mask Sampling

We further study the influence of SAM [22] masks sampling during the feature learning stage. We test three different

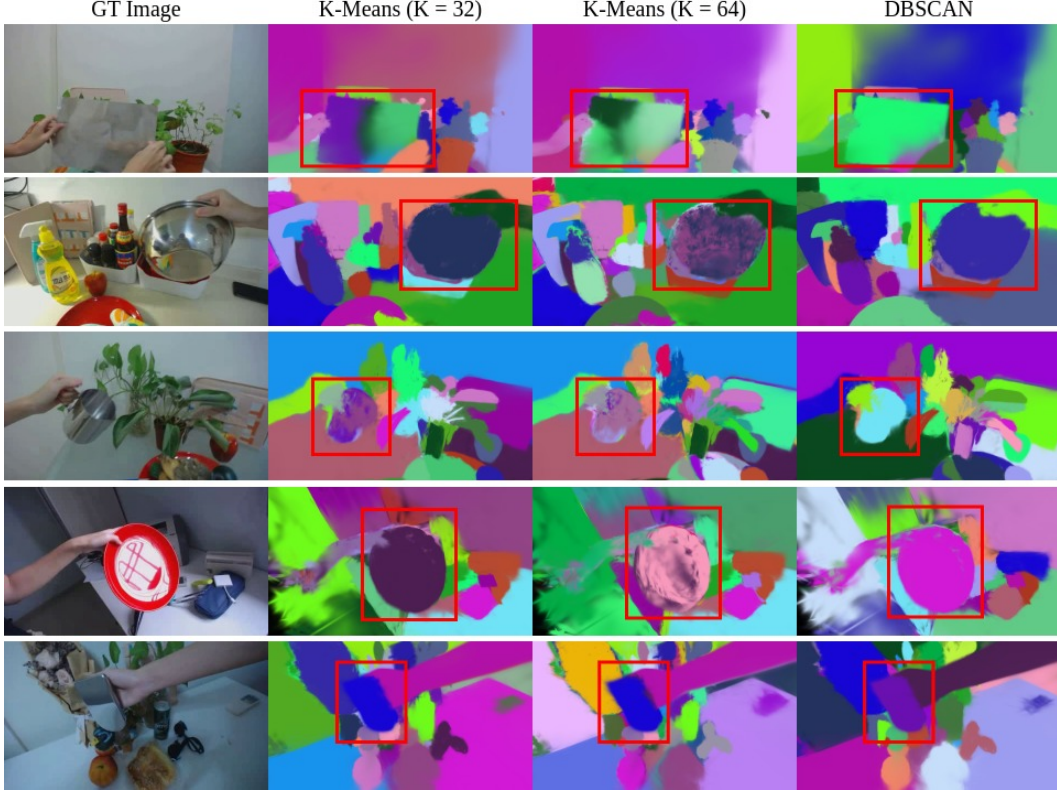


Figure 14. Comparison of rendered segmentation for K-Means (K=32), K-Means (K=64), and DBSCAN. K-Means-based segmentation results exhibit noise in the specular regions. Moreover, they require a pre-defined number of clusters, which is hard to provide for casual realistic videos. DBSCAN alleviates all of the above issues.

D	NeRF-DS-Mask		HyperNeRF-Mask		Neu3D-Mask	
	Size↓	Time↓	Size↓	Time↓	Size↓	Time↓
D=16	55	0.17	168	0.59	198	0.69
D=32 (Ours)	67	0.30	203	1.10	239	1.56
D=64	90	0.43	272	4.12	320	3.46
D=128	135	0.82	410	8.90	483	7.06

Table 9. Clustering time (second) and storage size (MB) analysis of different dimensionality of Gaussian features ($D \in \{16, 32, 64, 128\}$).

sampling heuristics: spatially uniform, based on the mask area (number of pixels), and based on the mask score. For the latter, we consider the stability scores from SAM [22] model, which reflects the reliability of the object against different object’s boundary changes. We have noticed many partial segments receiving high scores, especially for objects with reflective surfaces from the NeRF-DS dataset. This negatively affects the segmentation accuracy for the model that prioritizes the masks with the highest stability scores. Spatially uniform masks are retrieved by dividing the image space into 50 cells and sampling a mask per cell. If several candidates correspond to one cell, masks are selected based on their area. This method generally works well. However, true uniform sampling highly depends on

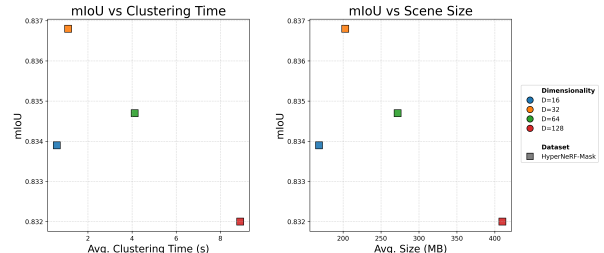


Figure 15. Scatter plot for the analysis of different Gaussian feature dimension $D \in \{16, 32, 64, 128\}$ on segmentation performance and runtime costs on HyperNeRF-Mask. **Left:** Comparison of mIoU against Average Clustering Time (seconds). **Right:** Comparison of mIoU against Average Scene Size (MB). The chosen configuration of $D = 32$ strikes a balance between model accuracy and computational requirements.

mask shape, size, and arrangement, which is hard to achieve with simple heuristics.

12. Limitations and Future Work

We observe that TRASE faces difficulties in separating small objects that significantly overlap with larger ones, as illustrated in Fig. 16. Intuitively, the scale-aware training

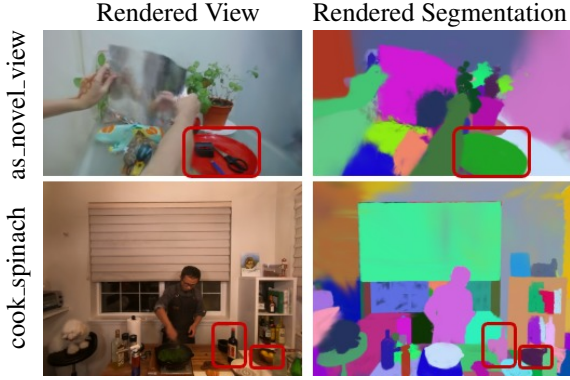


Figure 16. Examples of failure cases of TRASE on small and overlapping objects.

Method	NeRF-DS-Mask		HyperNeRF-Mask		Neu3D-Mask	
	intra (↓)	inter (↑)	intra (↓)	inter (↑)	intra (↓)	inter (↑)
TRASE (all)	0.2588	1.3756	0.3251	1.3382	0.2200	1.3894
TRASE (hard)	0.3517	1.1027	0.3488	1.1078	0.2942	1.2600
TRASE (Ours)	0.2538	1.3761	0.2437	1.3406	0.1752	1.3925

Table 10. Ablation study on our contrastive objective. We compare the mean intra- and inter-cluster distance with our soft mining strategy (Ours), sampling all positive–negative pairs (all) and sampling only pairs that individually satisfy the thresholds (hard).

proposed by SAGA [6] should improve the segmentation of these smaller objects; however, our experiments indicate that their pipeline yields noisy segmentation results. A potential alternative is to refine the construction of the mask-based correspondence matrix C . While the current implementation encodes it with binary values (0 or 1), employing soft or probabilistic values could offer greater robustness.

As described in the main paper, our method follows a two-stage training scheme. Thus, exploring the benefits of learning dynamic reconstruction and segmentation jointly is an exciting future direction of TRASE. Moreover, due to the rapid advances in the field, novel dynamic 3DGS reconstruction backbones can be combined with our soft-mining feature learning to achieve better segmentation performance.

13. Additional Evaluations of Soft-Mining Contrastive Objective

Soft vs. Hard vs. All Mining. To validate the effectiveness of our soft-mined pixel-pair sampling strategy, we compare its average intra-cluster and inter-cluster distances against two baselines: sampling all positive–negative pairs (all) and sampling only pairs that individually satisfy the thresholds (hard), as shown in Tab. 10. Our results show that soft sample mining reduces intra-cluster distances while increasing inter-cluster distances, thereby improving feature separability.

Comparison to Contrastive Methods. Existing con-

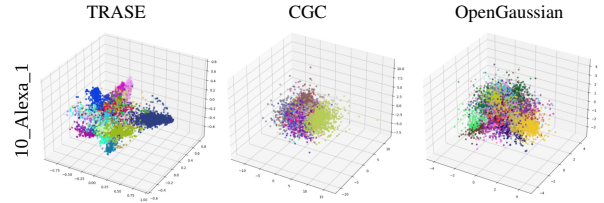


Figure 17. Feature space visualization with PCA of CGC [12], OpenGaussian [46], and TRASE on 10_Alexa_1 sequence. TRASE exhibits clearer separation between different clusters and a directional structure, which allows to preserve more meaningful variations within a cluster.

trastive segmentation methods CGC [12] and OpenGaussian [46] treat all negative pairs equally and focus on average feature consistency. However, this often leads to ambiguous feature assignments (Fig. 17) and segmentation artifacts (Fig. 18). In contrast, TRASE optimizes per-pixel relationships by introducing soft sample mining as discussed in our main paper.

It prioritizes challenging pixels that have any negative pixel pairs that are close in feature space and any positive pairs that are far apart, leading to more discriminative feature representations. We confirm our findings by evaluating segmentation accuracy in Tab. 1 (main). Our TRASE achieves the best segmentation performance across all tested benchmarks, validating the effectiveness of the learned segmentation field.

14. Additional Feature Space Visualizations

As shown in Fig. 17, TRASE demonstrates superior performance in separating different clusters apart compared to the existing contrastive learning approaches [42, 46]. We provide additional results in Fig. 20. The features learned by TRASE are more discriminative compared to other approaches.

15. Additional Out-of-FoV Visualizations

As shown in the main paper, TRASE with soft sample mining demonstrates superior performance in the out-of-FoV viewpoint to eliminate floating artifacts compared to TRASE with hard / all sample mining and the existing contrastive learning approaches [42, 46]. We provide additional results in Fig. 18.

16. Further Scene Editing Examples

We present further scene composite examples of TRASE in Fig. 24. We also compare the quality of object removal and scene composition with SA4D [19] in Fig. 25 and Fig. 26. While SA4D introduces ghostly artifacts in place of the re-

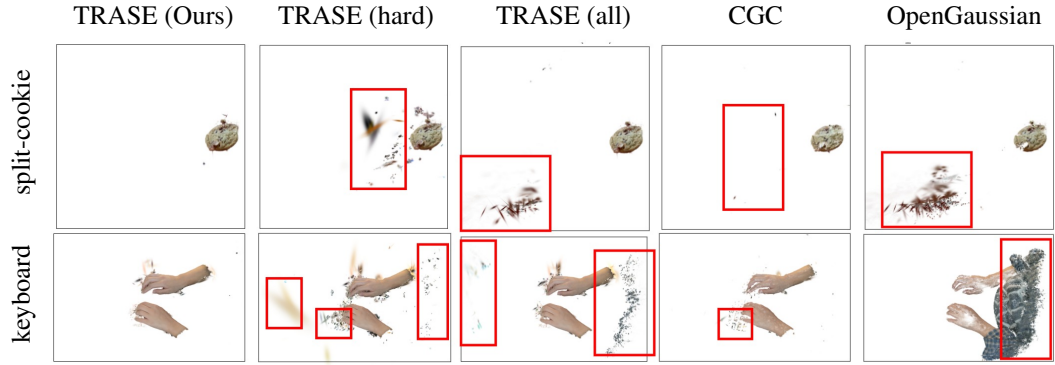


Figure 18. Additional results of out-of-FoV visualization from TRASE with soft sample mining (Ours), hard / all sample mining, CGC [42], and OpenGaussian [46].

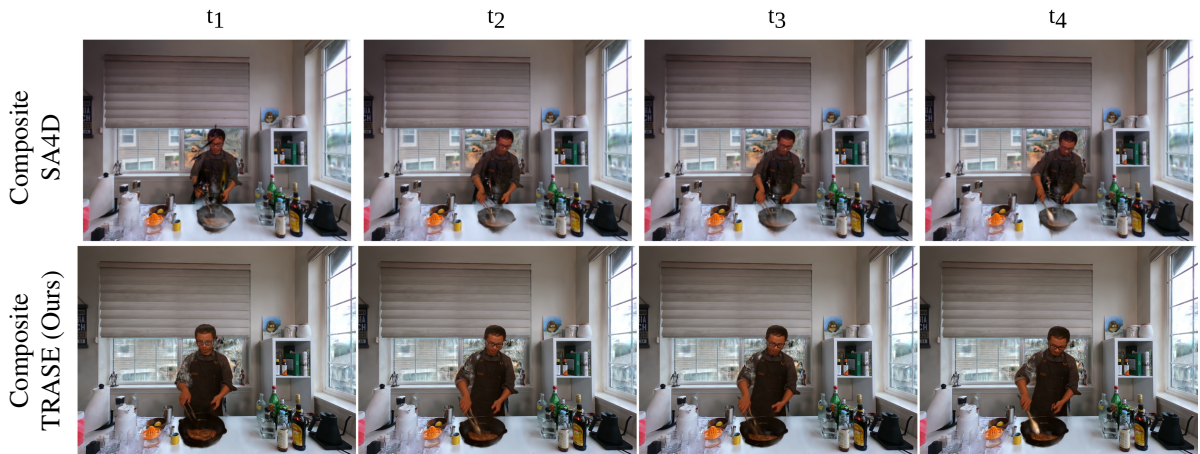


Figure 19. Scene composition with SA4D [19] and our TRASE on Neu3D sequences. We segment the person from *sear_steak* and replace him in *coffee_martini* with it. Our method delivers fewer artifacts. The scale and position of the object are adapted manually to fit the scene.

moved objects and carries spurious Gaussians with the segmented objects, our TRASE delivers photorealistic results of the edited scene.

17. Detailed Quantitative Results per Dataset

For completeness to the average numbers per datasets (main), we report the performance of our method individually on all benchmarks in Tab. 11, Tab. 12, Tab. 13, Tab. 14, and Tab. 15.

18. Additional Qualitative Results

We provide additional qualitative results in Fig. 21 and Fig. 22 to further showcase the effectiveness of TRASE over other methods. While SAGA [7] suffers from degenerate Gaussians, our reconstruction backbone and effective post-processing mitigate the issue. At the same time, rendered masks from other methods, such as DGD [24] and SA4D [19], are inaccurate and introduce spurious re-

gions. Our method demonstrates the best performance among all approaches. We also showcase in Fig. 23 that TRASE achieves both time and space consistency in multi-view video dataset such as Neu3D.

19. Visualization of the Rendered View, Rendered Segmentation, Segmented Object

We also provide the visualizations of the rendered novel view, the rendered segmentation, and the segmented objects in Fig. 27, Fig. 28, and Fig. 29. The rendered segmentation of TRASE is based on Gaussian clustering, which is performed in 3D space, resulting in consistent segmentation in the dynamic scene.

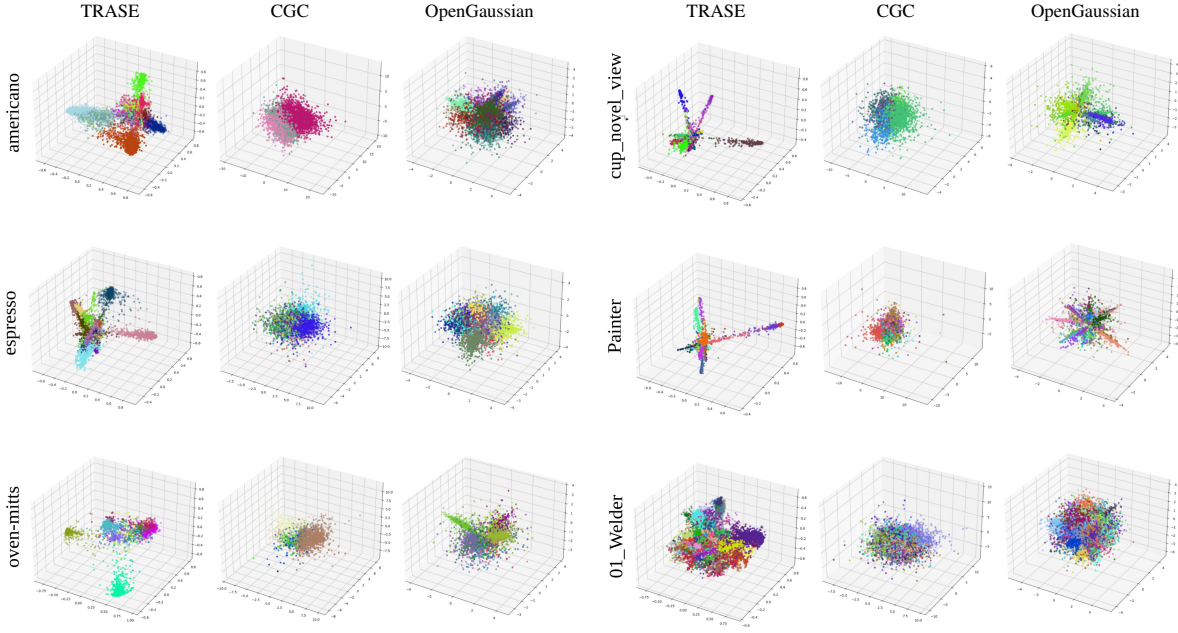


Figure 20. Additional results of feature space visualization from TRASE, CGC [42], and OpenGaussian [46]. Our method exhibits more compact clusters with more refined boundaries than other methods, which indicates high feature discrimination of our latent space.

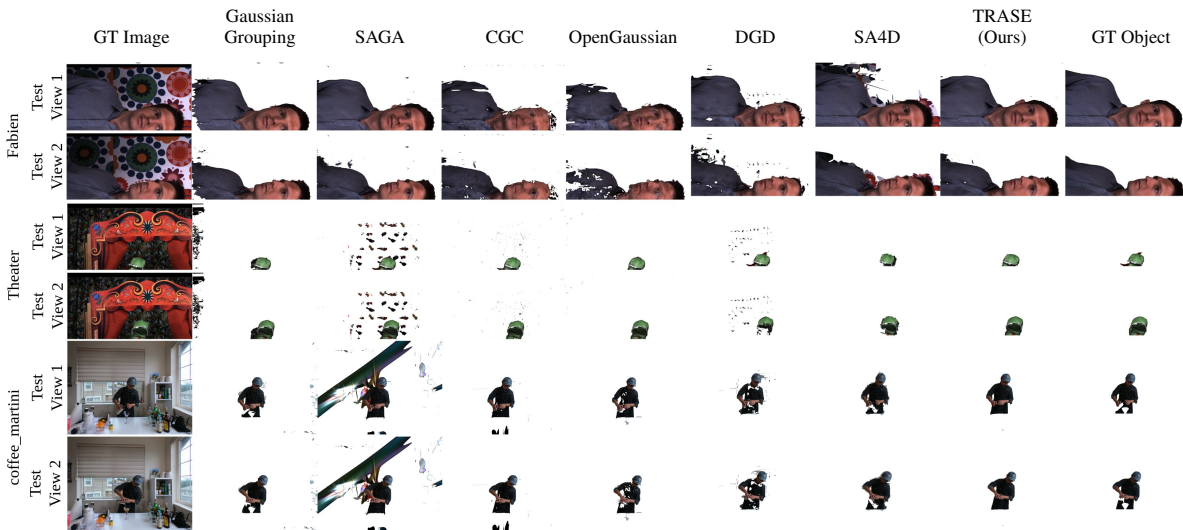


Figure 21. Segmentation qualitative results on *Technicolor-Mask* and *Neu3D-Mask* sequences. Our method delivers the best temporally consistent performance across all baselines. Please note that OpenGaussian is not evaluated on *Neu3D-Mask*.

Method	as_novel_view		basin_novel_view		cup_novel_view		press_novel_view		plate_novel_view		Average	
	mIoU	mAcc	mIoU	mAcc	mIoU	mAcc	mIoU	mAcc	mIoU	mAcc	mIoU	mAcc
Gaussian Grouping [53]	0.8140	0.9487	0.8083	0.9612	0.9020	0.9936	0.7803	0.9912	0.8710	0.9696	0.8351	0.9729
SAGA [6]	0.8235	0.9542	0.6437	0.9140	0.8833	0.9922	0.8119	0.9918	0.8736	0.9699	0.8072	0.9644
SA4D [19]	0.7384	0.9158	0.7663	0.9609	0.7759	0.9858	0.6558	0.9894	0.4337	0.8282	0.6740	0.9360
DGD [24]	0.7135	0.9266	0.6685	0.9291	0.694	0.9752	0.6457	0.9822	0.8406	0.9625	0.7125	0.9551
CGC [12]	0.7388	0.9404	0.8084	0.9659	0.8556	0.9908	0.7723	0.9905	0.8748	0.9716	0.8100	0.9718
OpenGaussian [46]	0.7471	0.9438	0.8580	0.9759	0.8406	0.9896	0.3047	0.9500	0.7191	0.9228	0.6939	0.9564
TRASE (Ours)	0.9160	0.9798	0.8704	0.9775	0.8893	0.9927	0.8257	0.9926	0.8826	0.9729	0.8768	0.9831

Table 11. Quantitative results for Gaussian Grouping [53], SAGA [6], SA4D [19], DGD [24], CGC [12], OpenGaussian [46] and TRASE on our *NeRF-DS-Mask* segmentation benchmark. TRASE outperforms the baselines on average.

Method	americano		chickchicken		cut-lemon1		espresso		hand		keyboard	
	mIoU	mAcc										
Gaussian Grouping [53]	0.8980	0.9969	0.9436	0.9867	0.7153	0.9394	0.4968	0.9642	0.8865	0.9814	0.9159	0.9861
SAGA [6]	0.7325	0.9873	0.8633	0.9648	0.5263	0.8398	0.6395	0.9798	0.9088	0.9859	0.8070	0.9645
SA4D [19]	0.8488	0.9941	0.8269	0.9553	0.8161	0.9688	0.4507	0.9640	0.7064	0.9462	0.7930	0.9651
DGD [24]	0.7748	0.9912	0.8317	0.9589	0.8583	0.9718	0.7240	0.9871	0.8936	0.9838	0.8451	0.9733
CGC [12]	0.7917	0.9915	0.8625	0.9672	0.8047	0.9605	0.7586	0.9898	0.7692	0.9646	0.8838	0.9810
OpenGaussian [46]	0.5739	0.9723	0.8309	0.9583	0.8369	0.9659	0.5949	0.9760	0.7687	0.9618	0.3848	0.8051
TRASE (Ours)	0.8144	0.9922	0.9308	0.9835	0.8795	0.9769	0.7164	0.986	0.9006	0.9849	0.8952	0.9827
oven-mitts												
Gaussian Grouping [53]	0.7420	0.9505	0.9095	0.9721	0.9134	0.9960	0.9196	0.9981	0.8341	0.9771		
SAGA [6]	0.8667	0.9766	0.7323	0.8960	0.8186	0.9906	0.7652	0.9933	0.7660	0.9579		
SA4D [19]	0.7257	0.9404	0.7205	0.8983	0.8351	0.9931	0.6474	0.9911	0.7371	0.9616		
DGD [24]	0.8595	0.9755	0.8408	0.9470	0.8467	0.9925	0.8223	0.9954	0.8297	0.9777		
CGC [12]	0.9025	0.9832	0.8378	0.9469	0.7975	0.9906	0.7488	0.9929	0.8157	0.9768		
OpenGaussian [46]	0.9107	0.9845	0.7470	0.9170	0.8816	0.9946	0.0011	0.9440	0.6531	0.9480		
TRASE (Ours)	0.9295	0.9876	0.8782	0.9617	0.8581	0.9930	0.8599	0.9964	0.8663	0.9845		

Table 12. Quantitative results for Gaussian Grouping [53], SAGA [6], SA4D [19], DGD [24], CGC [12], OpenGaussian [46] and TRASE on our *HyperNeRF-Mask* segmentation benchmark. TRASE outperforms the baselines on average.

Method	coffee_martini		cook_spinach		cut_roasted_beef		flame_steak		sear_steak		Average	
	mIoU	mAcc	mIoU	mAcc	mIoU	mAcc	mIoU	mAcc	mIoU	mAcc	mIoU	mAcc
Gaussian Grouping [53]	0.8295	0.9890	0.8974	0.9941	0.9512	0.9972	0.8279	0.9900	0.9261	0.9959	0.8864	0.9932
SAGA [6]	0.2201	0.8081	0.8125	0.9881	0.6982	0.9767	0.8439	0.9911	0.8959	0.9941	0.6941	0.9516
SA4D [19]	0.8583	0.9910	0.8987	0.9941	0.8645	0.9914	0.8898	0.9940	0.9047	0.9948	0.8832	0.9931
DGD [24]	0.7875	0.9865	0.8150	0.9883	0.8170	0.9877	0.6771	0.9776	0.7638	0.9854	0.7721	0.9851
CGC [12]	0.8359	0.9895	0.9034	0.9945	0.9052	0.9943	0.8530	0.9920	0.8794	0.9934	0.8754	0.9927
OpenGaussian [46]	0.8254	0.9896	0.6336	0.9798	0.9115	0.9951	0.8199	0.9907	0.8986	0.9943	0.8178	0.9899
TRASE (Ours)	0.9120	0.9948	0.9129	0.9951	0.9103	0.9947	0.8716	0.9930	0.9044	0.9947	0.9022	0.9945

Table 13. Quantitative results for Gaussian Grouping [53], SAGA [6], SA4D [19], DGD [24], CGC [12] and TRASE on our *Neu3D-Mask* segmentation benchmark. TRASE remains on par with Gaussian Grouping on average and outperforms SAGA by a large margin on average mIoU.

Method	01_Welder		02_Flames		10_Alexa_1		11_Alexa_2		Average	
	mIoU	mAcc								
Gaussian Grouping [53]	0.7920	0.9736	0.8364	0.9936	0.7391	0.9840	0.7018	0.9590	0.7673	0.9776
SAGA [6]	0.8062	0.9737	0.8463	0.9940	0.4794	0.9513	0.8260	0.9797	0.7395	0.9747
SA4D [19]	0.7728	0.9708	0.7200	0.9871	0.8351	0.9907	0.8669	0.9853	0.7987	0.9835
DGD [24]	0.873	0.9854	0.7775	0.9914	0.8107	0.9899	0.7312	0.9734	0.7981	0.9850
CGC [12]	0.911	0.9894	0.8520	0.9947	0.8464	0.9924	0.9328	0.9933	0.8856	0.9925
OpenGaussian [46]	0.9077	0.9891	0.1439	0.9419	0.8752	0.9941	0.9213	0.9922	0.7120	0.9793
TRASE (Ours)	0.8975	0.9877	0.8808	0.9955	0.9367	0.9970	0.9786	0.9979	0.9234	0.9945

Table 14. Quantitative results for Gaussian Grouping [53], SAGA [6], SA4D [19], DGD [24], CGC [12], OpenGaussian [46] and TRASE on our *Immersive-Mask* segmentation benchmark. TRASE outperforms the baselines on average mIoU by a large margin.

Method	Birthday		Fabien		Painter		Theater		Average	
	mIoU	mAcc								
Gaussian Grouping [53]	0.9324	0.9908	0.9406	0.9758	0.8759	0.9888	0.4428	0.9646	0.7979	0.9800
SAGA [6]	0.8541	0.9779	0.9371	0.9943	0.9670	0.9867	0.4071	0.9579	0.7913	0.9792
SA4D [19]	0.8322	0.9736	0.8709	0.9460	0.8070	0.9808	0.7984	0.9930	0.8271	0.9734
DGD [24]	0.7203	0.9573	0.9177	0.9667	0.7959	0.9788	0.6826	0.9885	0.7791	0.9728
CGC [12]	0.7951	0.9668	0.9163	0.9659	0.9668	0.9971	0.8443	0.9950	0.8806	0.9812
OpenGaussian [46]	0.7008	0.9458	0.8590	0.9438	0.8928	0.9908	0.9034	0.9971	0.8390	0.9694
TRASE (Ours)	0.8839	0.9833	0.9734	0.9889	0.9719	0.9976	0.8941	0.9969	0.9308	0.9917

Table 15. Quantitative results for Gaussian Grouping [53], SAGA [6], SA4D [19], DGD [24], CGC [12], OpenGaussian [46] and TRASE on our *Technicolor-Mask* segmentation benchmark. TRASE outperforms the baselines on average mIoU by a large margin.

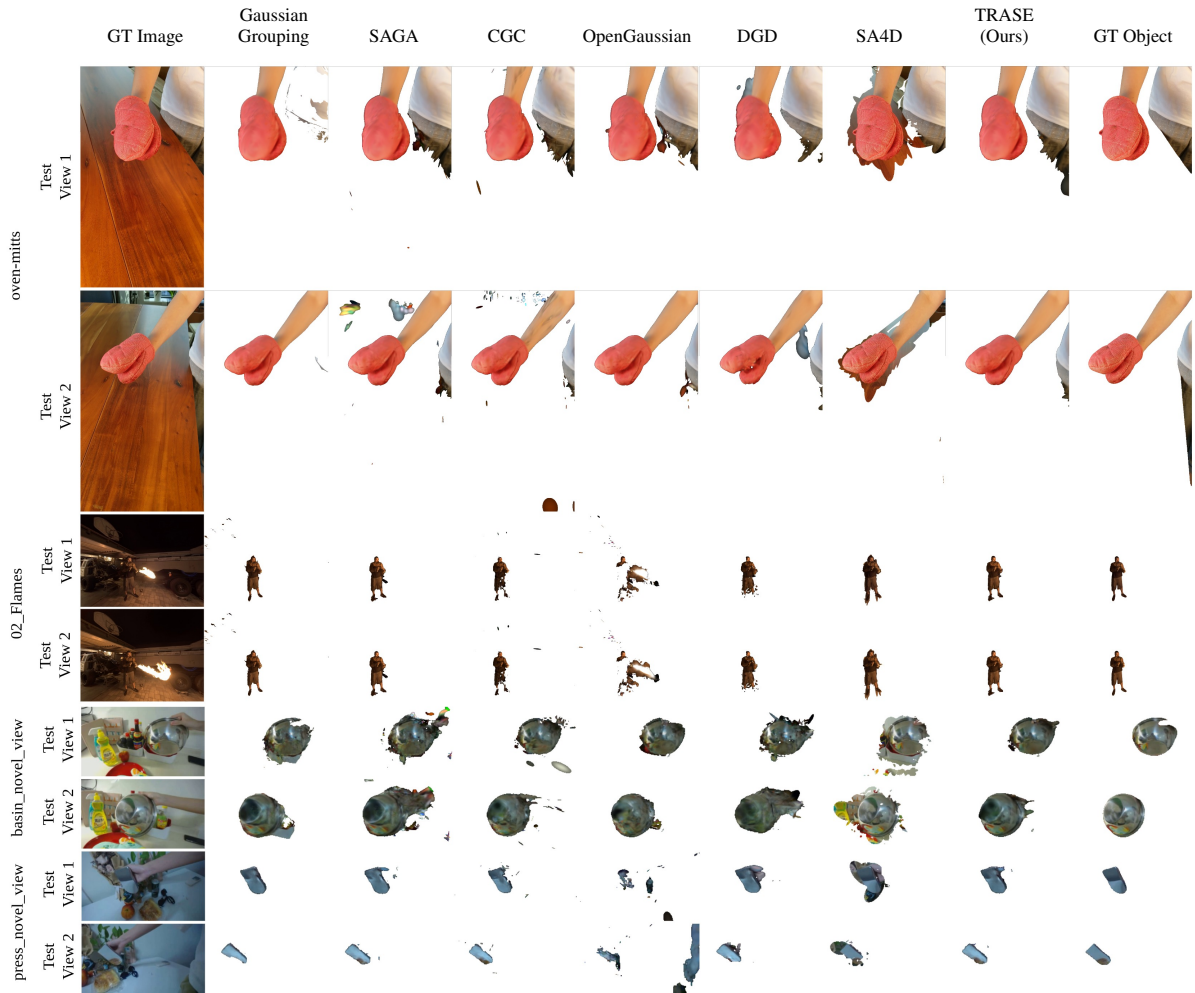


Figure 22. Segmentation qualitative results on *HyperNeRF-Mask*, *Immersive-Mask*, and *NeRF-DS-Mask* datasets. Our method delivers the best temporally consistent performance across all baselines.

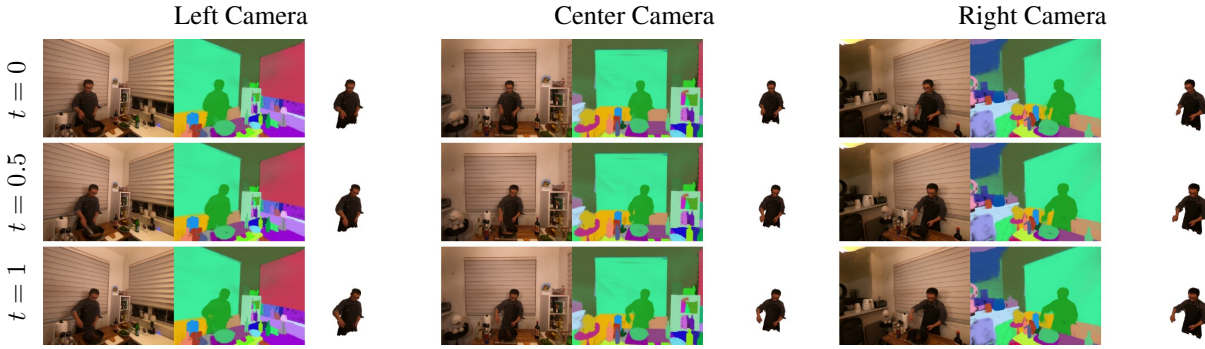


Figure 23. Visualization of the rendered scene from the left, center, and right camera. For each camera, we show the rendered view (left), rendered segmentation (middle), and segmented object (right). TRASE demonstrate multiview consistency in time and space.

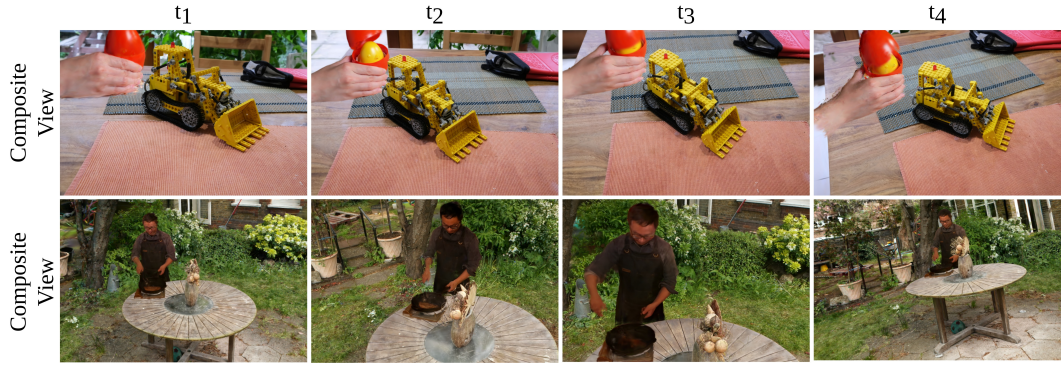


Figure 24. Scene composition with TRASE. Top: *chickchicken* and Mip-NeRF 360 [1] *kitchen*. Bottom: *sear_steak* and Mip-NeRF 360 [1] *garden*. The scale and position of the object are adapted manually to fit the scene.

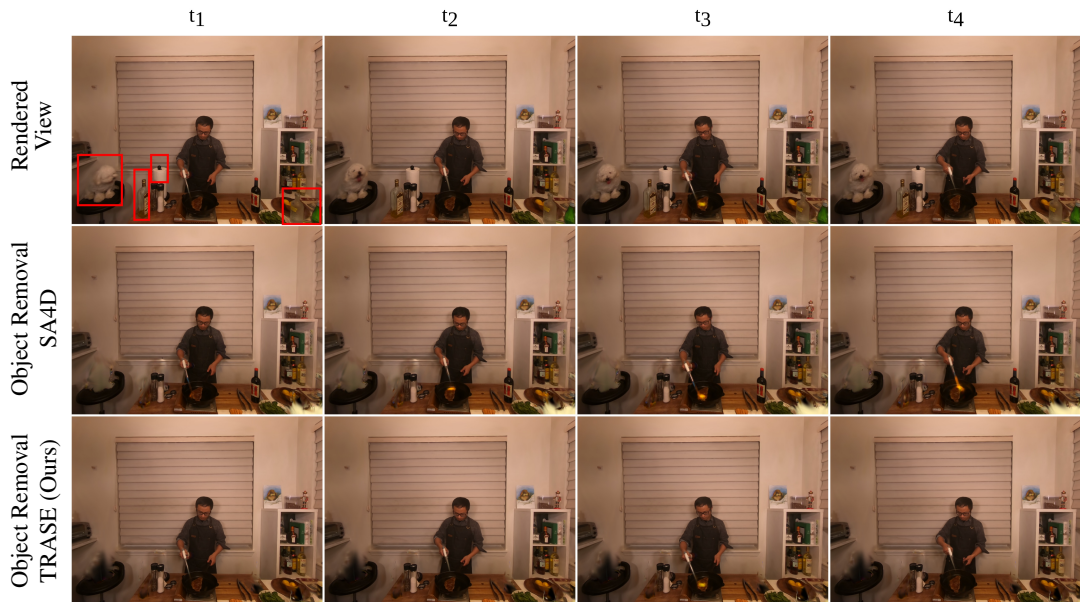


Figure 25. Object removal (identified with the red boxes) with SA4D [19] and our TRASE in Neu3D *flame_steak* sequence. Our method delivers fewer artifacts and does not introduce ghostly effects in place of the removed object.

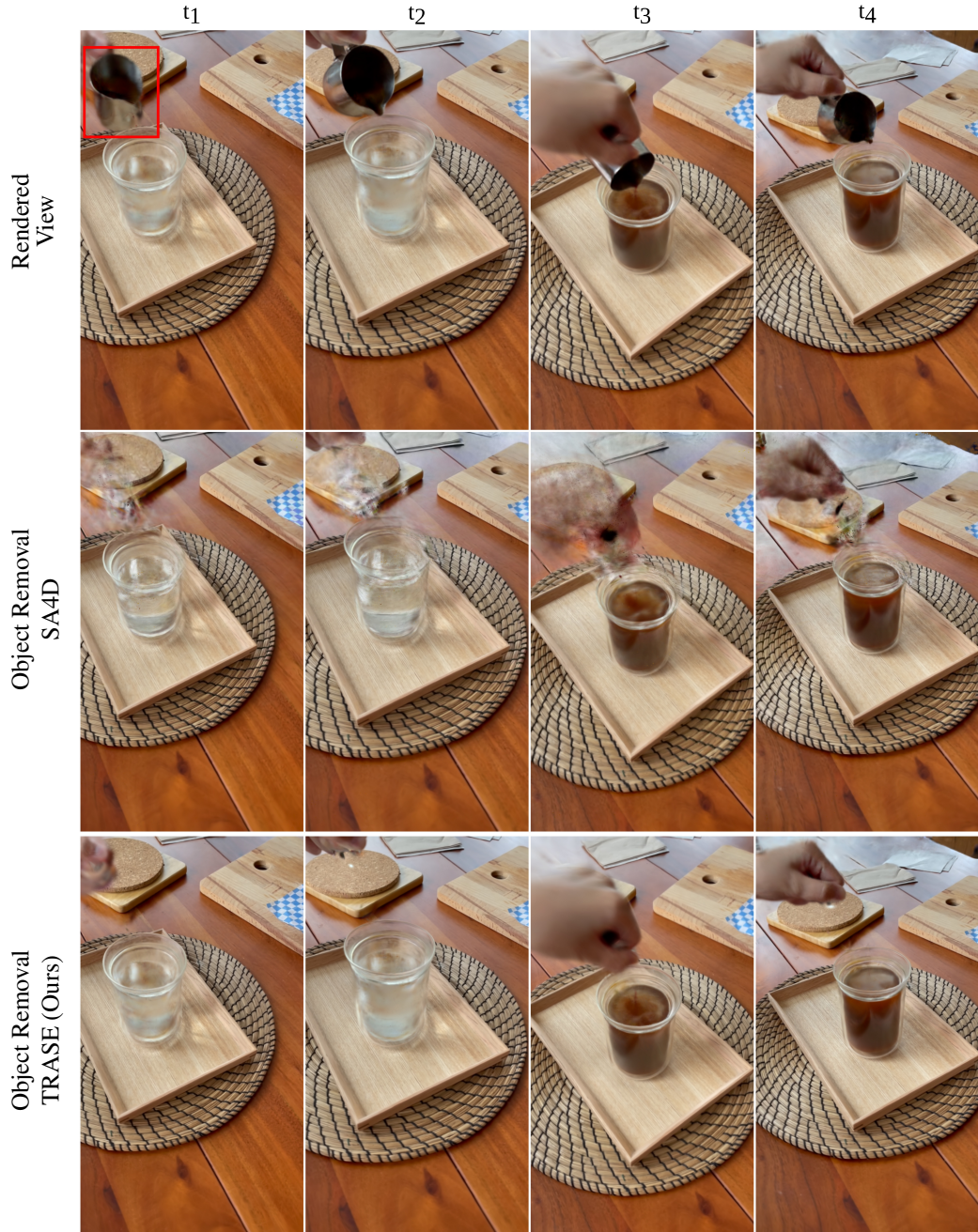


Figure 26. Object removal (saucer in the red box) with SA4D [19] and our TRASE in HyperNeRF *americano* sequence. Our method delivers fewer artifacts and does not introduce ghostly effects in place of the removed object. Our method does not require additional inpainting as the background is complete due to multi-view observations.

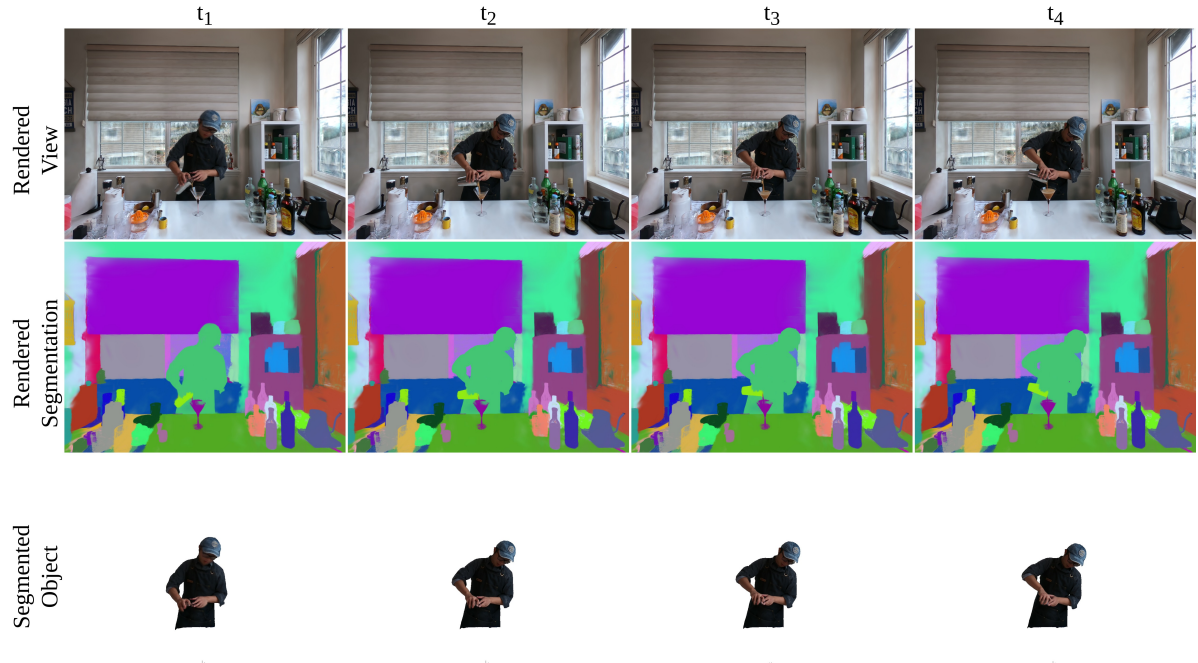


Figure 27. Visualization of rendered view, rendered segmentation, and segmented objects of the scene *coffee_martini* in four different timestamps in the novel views. The consistency of the semantic feature field across time opens out-of-box editing opportunities for dynamic scenes.

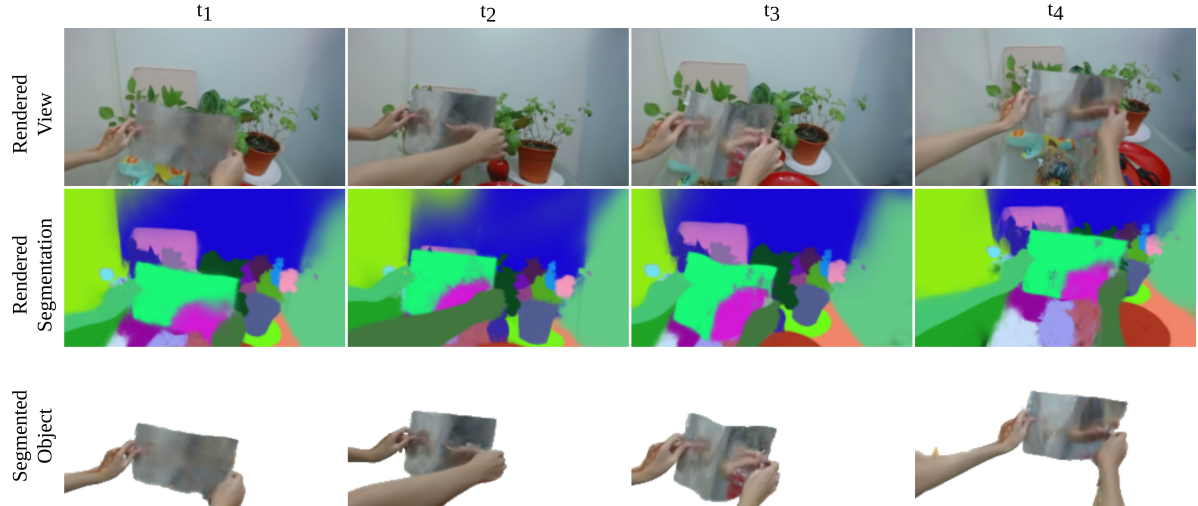


Figure 28. Visualization of rendered view, rendered segmentation, and segmented objects of the scene *as_novel_view* in four different timestamps in the novel views. The reflection in the foil remains temporally consistent, which enables post-processing editing effects.

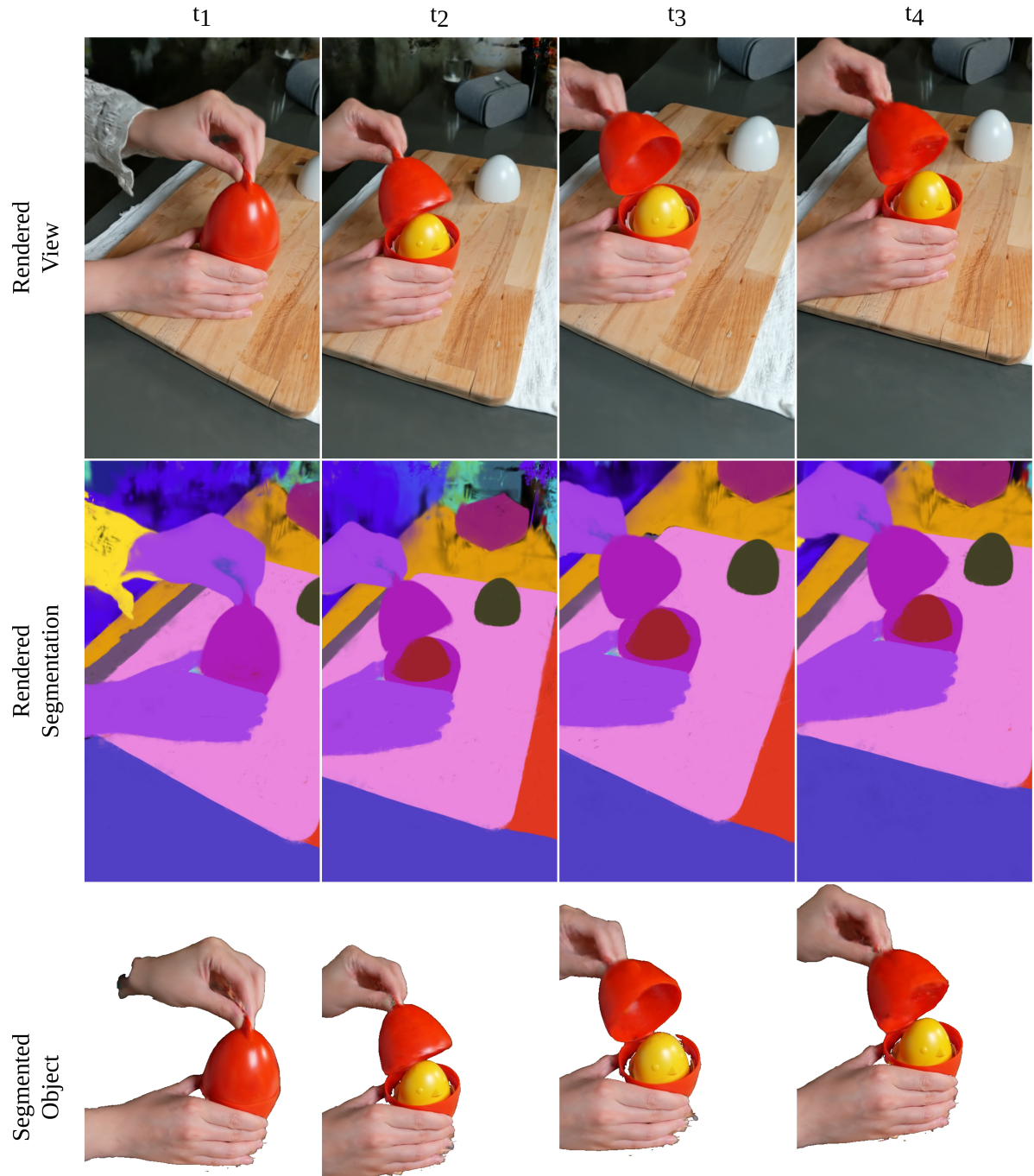


Figure 29. Visualization of rendered view, rendered segmentation, and segmented objects of the scene *chickchicken* in four different timestamps in the novel views. Despite severe occlusions, semantic segmentation is consistent over time.

References

[1] Jonathan T. Barron, Ben Mildenhall, Dor Verbin, Pratul P. Srinivasan, and Peter Hedman. Mip-nerf 360: Unbounded anti-aliased neural radiance fields. *CVPR*, 2022. 11

[2] Michael Broxton, John Flynn, Ryan Overbeck, Daniel Erickson, Peter Hedman, Matthew DuVall, Jason Dourgarian, Jay Busch, Matt Whalen, and Paul Debevec. Immersive light field video with a layered mesh representation. 39(4):86:1–86:15, 2020. 1

[3] Sergi Caelles, Alberto Montes, Kevins-Kokitsi Maninis, Yuhua Chen, Luc Van Gool, Federico Perazzi, and Jordi Pont-Tuset. The 2018 davis challenge on video object segmentation. *arXiv:1803.00557*, 2018. 2

[4] Sergi Caelles, Jordi Pont-Tuset, Federico Perazzi, Alberto Montes, Kevins-Kokitsi Maninis, and Luc Van Gool. The 2019 davis challenge on vos: Unsupervised multi-object segmentation. *arXiv:1905.00737*, 2019. 2

[5] Mathilde Caron, Hugo Touvron, Ishan Misra, Hervé Jégou, Julien Mairal, Piotr Bojanowski, and Armand Joulin. Emerging properties in self-supervised vision transformers. In *Proceedings of the IEEE/CVF international conference on computer vision*, pages 9650–9660, 2021. 2

[6] Jiazhong Cen, Jiemin Fang, Chen Yang, Lingxi Xie, Xiaopeng Zhang, Wei Shen, and Qi Tian. Segment any 3d gaussians. *arXiv preprint arXiv:2312.00860*, 2023. 1, 2, 4, 5, 6, 7, 9, 10

[7] Jiazhong Cen, Zanwei Zhou, Jiemin Fang, Wei Shen, Lingxi Xie, Dongsheng Jiang, Xiaopeng Zhang, Qi Tian, et al. Segment anything in 3d with nerfs. *Advances in Neural Information Processing Systems*, 36:25971–25990, 2023. 2, 7

[8] Ho Kei Cheng, Seoung Wug Oh, Brian Price, Alexander Schwing, and Joon-Young Lee. Tracking anything with decoupled video segmentation. In *Proceedings of the IEEE/CVF International Conference on Computer Vision*, pages 1316–1326, 2023. 2, 3, 6

[9] Thomas M. Cover and Peter E. Hart. Nearest neighbor pattern classification. *IEEE Transactions on Information Theory*, 13(1):21–27, 1967. 4

[10] Bin Dou, Tianyu Zhang, Yongjia Ma, Zhaohui Wang, and Zejian Yuan. Cosseggaussians: Compact and swift scene segmenting 3d gaussians. *arXiv preprint arXiv:2401.05925*, 2024. 3

[11] Martin Ester, Hans-Peter Kriegel, Jörg Sander, and Xiaowei Xu. A density-based algorithm for discovering clusters in large spatial databases with noise. In *Proceedings of the Second International Conference on Knowledge Discovery and Data Mining (KDD)*, pages 226–231, 1996. 2, 5

[12] Myrna C Silva et al. Contrastive gaussian clustering: Weakly supervised 3d scene segmentation. *arXiv preprint arXiv:2404.12784*, 2024. 2, 3, 5, 7, 6, 9, 10

[13] Yash Bhalgat et al. Contrastive lift: 3d object instance segmentation by slow-fast contrastive fusion. In *NeurIPS*, 2023. 2, 3

[14] Quankai Gao, Qiangeng Xu, Zhe Cao, Ben Mildenhall, Wenchao Ma, Le Chen, Danhang Tang, and Ulrich Neumann. Gaussianflow: Splatting gaussian dynamics for 4d content creation. 2024. 7

[15] Mariia Gladkova, Nikita Korobov, Nikolaus Demmel, Aljoša Ošep, Laura Leal-Taixé, and Daniel Cremers. Directtracker: 3d multi-object tracking using direct image alignment and photometric bundle adjustment. In *2022 IEEE/RSJ International Conference on Intelligent Robots and Systems (IROS)*, pages 3777–3784. IEEE, 2022. 7

[16] Michelle Guo, Alireza Fathi, Jiajun Wu, and Thomas Funkhouser. Object-centric neural scene rendering. *arXiv preprint arXiv:2012.08503*, 2020. 3

[17] Yongzhen Hu, Yihui Yang, Haotong Lin, Yifan Wang, Junting Dong, Yifu Deng, Xinyu Zhu, Fan Jia, Hujun Bao, Xiaowei Zhou, et al. Split4d: Decomposed 4d scene reconstruction without video segmentation. *ACM Transactions on Graphics (TOG)*, 44(6):1–15, 2025. 3

[18] Sahil Jain, Avik Kuthiala, Prabhdeep Singh Sethi, and Prakanshu Saxena. Stylesplat: 3d object style transfer with gaussian splatting, 2024. 8

[19] Shengxiang Ji, Guanjun Wu, Jiemin Fang, Jiazhong Cen, Taoran Yi, Wenyu Liu, Qi Tian, and Xinggang Wang. Segment any 4d gaussians. *arXiv preprint arXiv:2407.04504*, 2024. 1, 3, 5, 6, 7, 9, 10, 11, 12

[20] Bernhard Kerbl, Georgios Kopanas, Thomas Leimkühler, and George Drettakis. 3d gaussian splatting for real-time radiance field rendering. *ACM Transactions on Graphics*, 42(4), 2023. 1, 3, 4

[21] Chung Min Kim, Mingxuan Wu, Justin Kerr, Ken Goldberg, Matthew Tancik, and Angjoo Kanazawa. Garfield: Group anything with radiance fields. In *Proceedings of the IEEE/CVF Conference on Computer Vision and Pattern Recognition*, pages 21530–21539, 2024. 2

[22] Alexander Kirillov, Eric Mintun, Nikhila Ravi, Hanzi Mao, Chloe Rolland, Laura Gustafson, Tete Xiao, Spencer Whitehead, Alexander C Berg, Wan-Yen Lo, Piotr Dollar, and Ross B Girshick. Segment anything. *arXiv preprint arXiv:2304.02643*, 2023. 2, 3, 4, 8, 1, 5

[23] Abhijit Kundu, Kyle Genova, Xiaoqi Yin, Alireza Fathi, Caroline Pantofaru, Leonidas J Guibas, Andrea Tagliasacchi, Frank Dellaert, and Thomas Funkhouser. Panoptic neural fields: A semantic object-aware neural scene representation. In *Proceedings of the IEEE/CVF Conference on Computer Vision and Pattern Recognition*, pages 12871–12881, 2022. 3

[24] Isaac Labe, Noam Issachar, Itai Lang, and Sagie Benaim. Dgd: Dynamic 3d gaussians distillation, 2024. 1, 2, 3, 5, 6, 7, 9, 10

[25] Boyi Li, Kilian Q Weinberger, Serge Belongie, Vladlen Koltun, and René Ranftl. Language-driven semantic segmentation. *arXiv preprint arXiv:2201.03546*, 2022. 3

[26] Tianye Li, Mira Slavcheva, Michael Zollhoefer, Simon Green, Christoph Lassner, Changil Kim, Tanner Schmidt, Steven Lovegrove, Michael Goesele, Richard Newcombe, et al. Neural 3d video synthesis from multi-view video. In *Proceedings of the IEEE/CVF Conference on Computer Vision and Pattern Recognition*, pages 5521–5531, 2022. 1

[27] Stuart Lloyd. Least squares quantization in pcm. *IEEE transactions on information theory*, 28(2):129–137, 1982. 5, 4

[28] Jonathon Luiten, Georgios Kopanas, Bastian Leibe, and Deva Ramanan. Dynamic 3d gaussians: Tracking by persistent dynamic view synthesis. In *3DV*, 2024. 1, 4

[29] Weijie Lyu, Xuetong Li, Abhijit Kundu, Yi-Hsuan Tsai, and Ming-Hsuan Yang. Gaga: Group any gaussians via 3d-aware memory bank. *arXiv preprint arXiv:2404.07977*, 2024. 2, 3

[30] J. B. MacQueen. Some methods for classification and analysis of multivariate observations. In *Proceedings of the Fifth Berkeley Symposium on Mathematical Statistics and Probability*, pages 281–297. University of California Press, 1967. 5, 4

[31] Ben Mildenhall, Pratul P Srinivasan, Matthew Tancik, Jonathan T Barron, Ravi Ramamoorthi, and Ren Ng. Nerf: Representing scenes as neural radiance fields for view synthesis. *Communications of the ACM*, 65(1):99–106, 2021. 1

[32] Maxime Oquab, Timothée Darcet, Theo Moutakanni, Huy V. Vo, Marc Szafraniec, Vasil Khalidov, Pierre Fernandez, Daniel Haziza, Francisco Massa, Alaeldin El-Nouby, Russell Howes, Po-Yao Huang, Hu Xu, Vasu Sharma, Shang-Wen Li, Wojciech Galuba, Mike Rabbat, Mido Assran, Nicolas Ballas, Gabriel Synnaeve, Ishan Misra, Herve Jegou, Julien Mairal, Patrick Labatut, Armand Joulin, and Piotr Bojanowski. Dinov2: Learning robust visual features without supervision, 2023. 1, 2, 3

[33] Keunhong Park, Utkarsh Sinha, Peter Hedman, Jonathan T Barron, Sofien Bouaziz, Dan B Goldman, Ricardo Martin-Brualla, and Steven M Seitz. Hypernerf: A higher-dimensional representation for topologically varying neural radiance fields. *arXiv preprint arXiv:2106.13228*, 2021. 1

[34] Adam Paszke, Sam Gross, Francisco Massa, Adam Lerer, James Bradbury, Gregory Chanan, Trevor Killeen, Zeming Lin, Natalia Gimelshein, Luca Antiga, et al. Pytorch: An imperative style, high-performance deep learning library. *Advances in neural information processing systems*, 32, 2019. 1

[35] F. Perazzi, J. Pont-Tuset, B. McWilliams, L. Van Gool, M. Gross, and A. Sorkine-Hornung. A benchmark dataset and evaluation methodology for video object segmentation. In *Computer Vision and Pattern Recognition*, 2016. 2

[36] Jordi Pont-Tuset, Federico Perazzi, Sergi Caelles, Pablo Arbeláez, Alexander Sorkine-Hornung, and Luc Van Gool. The 2017 davis challenge on video object segmentation. *arXiv:1704.00675*, 2017. 2

[37] Alec Radford, Jong Wook Kim, Chris Hallacy, Aditya Ramesh, Gabriel Goh, Sandhini Agarwal, Girish Sastry, Amanda Askell, Pamela Mishkin, Jack Clark, et al. Learning transferable visual models from natural language supervision. In *International conference on machine learning*, pages 8748–8763. PMLR, 2021. 3

[38] Nikhila Ravi, Valentin Gabeur, Yuan-Ting Hu, Ronghang Hu, Chaitanya Ryali, Tengyu Ma, Haitham Khedr, Roman Rädle, Chloe Rolland, Laura Gustafson, Eric Mintun, Junting Pan, Kalyan Vasudev Alwala, Nicolas Carion, Chao-Yuan Wu, Ross Girshick, Piotr Dollár, and Christoph Feichtenhofer. Sam 2: Segment anything in images and videos. *arXiv preprint arXiv:2408.00714*, 2024. 3, 5, 1

[39] Tianhe Ren, Shilong Liu, Ailing Zeng, Jing Lin, Kunchang Li, He Cao, Jiayu Chen, Xinyu Huang, Yukang Chen, Feng Yan, et al. Grounded sam: Assembling open-world models for diverse visual tasks. *arXiv preprint arXiv:2401.14159*, 2024. 8

[40] Neus Sabater, Guillaume Boisson, Benoit Vandame, Paul Kerbiriou, Frederic Babon, Matthieu Hog, Remy Gendrot, Tristan Langlois, Olivier Bureller, Arno Schubert, et al. Dataset and pipeline for multi-view light-field video. In *Proceedings of the IEEE conference on computer vision and pattern recognition Workshops*, pages 30–40, 2017. 1

[41] Johannes Lutz Schönberger and Jan-Michael Frahm. Structure-from-motion revisited. In *Conference on Computer Vision and Pattern Recognition (CVPR)*, 2016. 2

[42] Myrna C. Silva, Mahtab Dahaghin, Matteo Toso, and Alessio Del Bue. Contrastive gaussian clustering: Weakly supervised 3d scene segmentation. <https://arxiv.org/abs/2404.12784>, 2024. 6, 7, 8

[43] Karen Simonyan and Andrew Zisserman. Very deep convolutional networks for large-scale image recognition. In *ICLR*, 2015. 8

[44] Vadim Tschernezki, Iro Laina, Diane Larlus, and Andrea Vedaldi. Neural feature fusion fields: 3d distillation of self-supervised 2d image representations. In *2022 International Conference on 3D Vision (3DV)*, pages 443–453. IEEE, 2022. 3

[45] Can Wang, Menglei Chai, Mingming He, Dongdong Chen, and Jing Liao. Clip-nerf: Text-and-image driven manipulation of neural radiance fields. In *Proceedings of the IEEE/CVF Conference on Computer Vision and Pattern Recognition*, pages 3835–3844, 2022. 1, 3

[46] Yanmin Wu, Jiarui Meng, Haijie Li, Chenming Wu, Yahao Shi, Xinhua Cheng, Chen Zhao, Haocheng Feng, Errui Ding, Jingdong Wang, et al. Opengaussian: Towards point-level 3d gaussian-based open vocabulary understanding. *Advances in Neural Information Processing Systems*, 37:19114–19138, 2025. 3, 5, 6, 7, 8, 9, 10

[47] Ning Xu, Linjie Yang, Yuchen Fan, Dingcheng Yue, Yuchen Liang, Jianchao Yang, and Thomas S. Huang. Youtub-evos: A large-scale video object segmentation benchmark. *CoRR*, abs/1809.03327, 2018. 2

[48] Zhiwen Yan, Chen Li, and Gim Hee Lee. Nerf-ds: Neural radiance fields for dynamic specular objects. In *Proceedings of the IEEE/CVF Conference on Computer Vision and Pattern Recognition*, pages 8285–8295, 2023. 6, 1

[49] Bangbang Yang, Yinda Zhang, Yinghao Xu, Yijin Li, Han Zhou, Hujun Bao, Guofeng Zhang, and Zhaopeng Cui. Learning object-compositional neural radiance field for editable scene rendering. In *Proceedings of the IEEE/CVF International Conference on Computer Vision*, pages 13779–13788, 2021. 3

[50] Linjie Yang, Yuchen Fan, and Ning Xu. The 2nd large-scale video object segmentation challenge - video object segmentation track, 2019. 2

[51] Linjie Yang, Yuchen Fan, and Ning Xu. The 4th large-scale video object segmentation challenge - video object segmentation track, 2022. 2

- [52] Ziyi Yang, Xinyu Gao, Wen Zhou, Shaohui Jiao, Yuqing Zhang, and Xiaogang Jin. Deformable 3d gaussians for high-fidelity monocular dynamic scene reconstruction. In *Proceedings of the IEEE/CVF Conference on Computer Vision and Pattern Recognition*, pages 20331–20341, 2024. [1](#), [2](#), [3](#), [4](#), [8](#)
- [53] Mingqiao Ye, Martin Danelljan, Fisher Yu, and Lei Ke. Gaussian grouping: Segment and edit anything in 3d scenes. 2024. [1](#), [2](#), [3](#), [5](#), [6](#), [7](#), [8](#), [9](#), [10](#)
- [54] Haiyang Ying, Yixuan Yin, Jinzhi Zhang, Fan Wang, Tao Yu, Ruqi Huang, and Lu Fang. Omniseg3d: Omniversal 3d segmentation via hierarchical contrastive learning. In *Proceedings of the IEEE/CVF Conference on Computer Vision and Pattern Recognition*, pages 20612–20622, 2024. [2](#), [3](#)
- [55] Kai Zhang, Nick Kolkin, Sai Bi, Fujun Luan, Zexiang Xu, Eli Shechtman, and Noah Snavely. Arf: Artistic radiance fields. In *European Conference on Computer Vision*, pages 717–733. Springer, 2022. [8](#)
- [56] Shijie Zhou, Haoran Chang, Sicheng Jiang, Zhiwen Fan, Zehao Zhu, Dejia Xu, Pradyumna Chari, Suya You, Zhangyang Wang, and Achuta Kadambi. Feature 3dgs: Supercharging 3d gaussian splatting to enable distilled feature fields. In *Proceedings of the IEEE/CVF Conference on Computer Vision and Pattern Recognition*, pages 21676–21685, 2024. [3](#), [4](#)